New plasma diagnosis tables of hydrogen Stark broadening including ion dynamics

Marco A Gigosos† and Valentín Cardeñoso‡

† Departamento de Óptica, Universidad de Valladolid, 47071 Valladolid, Spain
‡ Departamento de Informática, Universidad de Valladolid, 47071 Valladolid, Spain

Abstract. A set of tables of the Stark width of the first three lines of Lyman and Balmer series of hydrogen, useful for plasma diagnosis purposes, is presented in this work. These tables have been obtained by means of a fully recognized computer simulation technique. Computer experiments have been carried out for density values between 10^{20} m^{-3} and $10^{24.67}$ m^{-3}. Simulation temperatures range from 2245 K to 224 856 K. Ion dynamics effects are taken into account in a natural way and the most significative gas mixtures have been covered in the simulations, carried out at the reduced mass of the emitter–perturber pair $\mu = 0.5$, 0.6, 0.8, 0.9, 1.0, 1.25, 1.5, 1.75 and 2.0. A detailed discussion of the influence of the relevant plasma parameters on the characteristics of the profiles is also included. The results show an excellent agreement with up-to-date experimental results and confirm these kind of profile calculation techniques as now the most accurate.

1. Introduction

The analysis of Stark-broadened spectral-line profiles is one of the most common methods of plasma diagnosis from the beginning of the sixties. The shape of these profiles depends heavily on the density of charged particles surrounding the emitter. This dependence is specially important in hydrogen and hydrogenic ions, since in those elements a linear Stark effect takes place. As a consequence, Stark-broadening measurements have become one of the most widely used techniques when plasma electron density is to be determined. On the other hand, accurate knowledge of the shapes of the line profiles are mandatory in order to determine the opacity spectral distribution. These kind of diagnostics play a key role in astrophysics, where active spectroscopy is not possible.

To this end, profile tables of hydrogen Stark broadening have been in use since the beginning of the seventies [1, 2]. The calculations leading to these tables were made in the framework of a plasma model in which it is assumed that the broadening of the lines can be computed as a sum of the contributions of all the collisions of a statistical ensemble of quasi-independent charged particles with the emitting atom. Depending on the speed of the perturbing particles, two different approximations were considered in order to simplify the computation of the contribution of each of the two different broadening mechanisms which are taken into account: it is assumed that the highly mobile electrons are responsible for sudden variations in the phase of the emitted wave—impact regime—while the heavier and slower ions generate electric fields which can be considered constant along the life of a typical emission—quasistatic regime.

Soon after the publication of these tables, it was shown experimentally that the movement of the perturbing ions plays a key role in order to explain the shape of the central region of Stark-broadened profiles [3–9], specially at low-density values. This was specially true for the central dip of beta lines and gamma's characteristic shoulder, where the experiments showed much less structure than predicted by the theories. Also, the experimental values of the width of alpha lines were clearly higher than the ones found in the tables, specially at low electron densities where discrepancies even exceed the order of magnitude. Nevertheless, the width of the Balmer beta line was revealed as the most interesting parameter for diagnostic purposes, since it was almost insensitive to the ion dynamics effects. Balmer beta line width was shown to be an accurate means of electron density calibration even for densities as low as 10^{20} m^{-3}.

Not without discussion, all these differences were finally attributed to ion dynamics effects. In fact, it was shown that an extrapolation of the experimental results to the static perturber case gives values of the characteristic elements of the profiles which are very similar to the ones found in the tables [5]. If the ion-emitter reduced mass μ is assumed to be the relevant parameter of the relative movement of emitter and perturbers, that extrapolation corresponds with the static ions situation, $\mu = \infty$.

While these experimental results were obtained, other Stark-broadening calculation methods were developed. Starting from the work of Frisch and Brissaud [10], Seidel was able to obtain theoretical profiles of hydrogen lines which included ion dynamics effects by means of the so-called model microfield method (MMM) [11]. The evolution of the electric microfield seen by the emitter is the key object in this calculation. The temporal behaviour of this microfield can be readily guessed from some heuristic considerations [12] and, by this means, one can make a homogeneous treatment of the dynamic effects of ions and electrons, thus including the contribution of ion dynamics.

Finally, a new profile calculation era was started in the eighties, when the computer-simulation paradigm was first applied to the field [13–20]. Properly speaking, none of these calculations introduced new plasma models, since they were all based in the same suite of physical considerations as the previous theoretical ones: the broadening is produced by the joint action of ions and electrons colliding with the emitting particle and the plasma is made of quasi-independent particles, although a partial account of correlation can be given by means of screened fields and cut-off parameters. Nonetheless, these techniques allowed us to properly include, for the first time, all those effects which had been known to all the previous treatments but could only be handled under sometimes severe approximations: collision overlapping effects, time ordered integrals, ion movement, etc. At the same time, it was shown that the effect of electrons and ions could be handled in exactly the same way, provided one could devise an adequate rewriting of the fundamental equation compatible with a reasonable amount of computing power. Computer-simulation techniques also allow experimentation with isolated physical effects, as it would in an ideal laboratory [21]. Molecular-dynamics simulation were also the basis of several semianalytical computations. In this case, a computer simulation was carried out in order to get an electric field from which several statistical parameters could be extracted and used in the analytical evaluation of the final spectral profiles [22–26].

Computer-simulation results have played a fundamental role in the assessment of the observed discrepancies between the experimental and the previous theoretical results and have reinforced the fact that they have to do with ion dynamics effects. Also, these techniques have revealed themselves as the most accurate means of computation of the spectral lineshapes. The high quality and confidence of the results in the density and temperature ranges covered by the calculations have shown that the physical model of the

simulated plasma is accurate enough for electron densities between 10^{20} m^{-3} and 10^{24} m^{-3} and temperatures of up to 10^7 K [15]. As for the μ-ion model itself, it is essential for simulation purposes because, thanks to it, just the movement of the perturbers has to be considered in order to give account of the joint movement of the emitter–perturber pairs. It has been more than 10 years since Seidel and Stamm [14] showed that this approximation is good enough for diagnostic purposes while it allows easier and more computer-tractable calculations, because thermal and Stark effects are considered to be statistically independent—which means that the final line profile can be obtained by a simple convolution of the Stark and Doppler part.

The state of the art in computer simulations and the quality of their results has led some authors to pose the need to obtain new Stark-broadening tables for hydrogenic elements using these kinds of methods [27]. In the course of this work the authors will show that this need can be fairly fulfilled by means of an updated version of the plasma-simulation technique they presented some time ago. These tables aim to provide a useful practical tool in plasma diagnosis using hydrogen Stark profiles.

The range of temperatures and electron densities covered in this work is the widest one in up-to-date computer simulated line profiles and it has been chosen so as to balance two opposite facts: it should be as wide as possible to be useful both at high and low densities but it has to be within reasonable limits so that the fundamental physical model is still valid. Since fine structure effects have not been taken into account in this work, the result for the lower densities should be taken with some reserve. The inclusion of such a phenomenon would have implied the lack of such an efficient integration mechanism as the one we have used and, although it is not out of the way that this kind of effect could be efficiently considered, it seemed more sensible to try to get diagnostic tables using a well known method, specially if the final results are to be useful in everyday experiments. Anyway, the comparison of our results with the predictions of some other models and with experimental data show that even for the lowest densities covered in this work they can be confidently used for diagnostic purposes, as shall be discussed later on.

For the sake of completeness, the details of the profile-computation method will be presented in the following section. Although part of them have already been quoted in previous works, it has never been discussed in such a systematic and thorough way. This exposition should be most valuable for everyone, specially if a practical use of the results is going to be made.

2. Computation procedure of the spectral lineshapes

The profile of a spectral line can be readily obtained from the autocorrelation function of the atomic dipole momentum by means of a Fourier transform of its average { } over a certain statistical ensemble [2]

$$I(\omega) = \frac{1}{\pi} \operatorname{Re} \int_0^\infty e^{-i\omega t} \{C(t)\}, \tag{1}$$

$$C(t) = \operatorname{tr}(\boldsymbol{D} \cdot U^+(t) \boldsymbol{D} U(t)). \tag{2}$$

The dipole momentum operator $\boldsymbol{D}$ has all the quantum information about the atomic transition under study. The trace of the matrix that appears in (2) represents the quantum average over the set of states of the emitter. The time development operator $U(t)$ obeys the following form of the Schrödinger equation under the *no-quenching* approximation:

$$i\hbar \frac{d}{dt} U(t) = V(t)U(t), \tag{3}$$

$$V(t) = q\mathbf{E}(t) \cdot \mathbf{R}, \tag{4}$$

where $q\mathbf{R}$ is the dipole momentum operator of the emitter and $\mathbf{E}(t)$ is the electric microfield generated by ions and electrons surrounding it.

In a computer-simulation process, a microfield time sequence is obtained for some selected plasma conditions and the numerical integration of equations (3) is a previous step to the calculation of $\{C(t)\}$, whose Fourier transform gives the final line profile.

In this work we have used a variation of the simulation techniques presented in previous papers [17, 20, 28]. The basics of these techniques and the improvements introduced in this work will be presented in the following sections.

2.1. Simulation process

The simulated plasma is an electrically neutral ensemble of statistically independent charged particles made of N_p ions and N_p electrons moving almost at random within a spherical box. An emitter is assumed to be placed at the centre of such a box. All the values of the spatial magnitudes are measured in terms of the mean interparticle distance R_0 which depends on the perturber density N_e ($R_0 = (\frac{3}{4}\pi N_e)^{1/3}$). Temporal evolution of the whole system is measured along a discrete time axis from zero to a definite number of times of a fixed increment—simulation time step. The total number of time steps can be chosen in a semi-empirical way from the total width at half height of the line that is being calculated. In this way, the evolution of the system can be defined as a sequence of temporal states. Every temporal state is given by the set of values of the positions and velocities of the particles in the system.

The position of every perturber can be given in terms of its impact parameter value b, its velocity v and the impact parameter crossing time t_0. Statistical distributions for these parameters should be chosen that ensure plasma homogeneity and isotropy and a Maxwell distribution of the kinetic energy of the ensemble in terms of the relative speed of the emitter–perturber pair, according to the μ-ion model [14].

In order to fix the initial conditions of the particles of every species, the impact parameter axis is divided into N_p cells of equal probability according to the probability density function for b. The value of b for every particle is randomly chosen from this cell in a one-to-one fashion using the law

$$P(b)\,\mathrm{d}b = \frac{3}{R^3}b\sqrt{R^2 - b^2}\,\mathrm{d}b, \tag{5}$$

where R represents the simulation-sphere radius which in units of R_0 equals $R = N_p^{1/3}$. This means that the value of the impact parameter for the kth particle is given by

$$b_k = \sqrt{N_p^{2/3} - (N_p - k + x)^{2/3}} \tag{6}$$

where x is a uniform pseudorandom number in $(0, 1]$.

The speed of every particle is obtained by a similar procedure: the interval $(0, +\infty)$ is divided into $1 + N_p$ cells of equal probability according to a Maxwell distribution and a set of N_p values are randomly generated so that no cell contains more than one particle speed. Since the order of speed assignment is random, the index of the empty cell will be a stochastic variable and there will be no correlation effects between v and b values, as will be discussed in the following.

The two angles defining the collision plane of every perturber are randomly generated so that space isotropy is preserved. To obtain the definitive value of the initial position of the particle, a uniform distribution is used for the impact parameter crossing time.

In the simulation process, particles move along straight-line trajectories with constant speed. This means that several of these perturbers will eventually exit the simulation box and should be re-injected in order to keep density constant in time. The particle substitution technique is a crucial part of any simulation and special care should be taken in order to ensure stability of the various probability distribution functions. When a particle exits the sphere in our simulation model, it is substituted by another one according to the following rules.

(i) Its initial position is a random point on the surface of the sphere.

(ii) A new impact parameter value is drawn within the same cell as the exiting particle, using the distribution law (5). This avoids the particles progressively migrating to a neighbourhood of the sphere surface, as was shown in [17].

(iii) Using a Maxwell distribution, the speed of the new particle is drawn from the speed cell that was empty at the time. This ensures a different value of the bv product and avoids $b : v$ correlation. Of course, the new empty cell is the one occupied by the exiting particle. This criterion also avoids the plasma progressively cooling as the particles are replaced: only a narrow speed interval, randomly distributed within the axis $(0, +\infty)$, has no particle in it at any time.

(iv) The space orientation of the new trajectory is chosen at random, according with the restrictions imposed by the values already drawn for b and v: it will lay on the cone given by the entry point at the sphere surface and the inner sphere of radius b.

This substitution technique guarantees the stability of all the relevant statistical distributions along the lifetime of the simulation process [17]. It is worth pointing out here that the technique just described differs from the one in [20] in the use of an *empty* cell in the speed axis. This avoids the unwanted $b : v$ correlation which appeared in the procedure described in that work, in which the modulus of the velocity was maintained all along the simulation process.

At every time step, the electric field produced by ions and electrons is calculated using Debye screened field formulae in order to account, at least approximately, for the correlation effects between species of different charge.

In the simulation process, *natural* units are used: mean interparticle distance R_0 as unit length, $q/4\pi\epsilon_0 R_0^2$ as electric field unit and R_0/v_0 as unit time, v_0 being the mean squared speed of the given species ($v_0 = \sqrt{2kT/m}$). In this sense, the numeric simulation process does not depend on the temperature and electronic density N_e. However, the electric field generated by the perturbers depends on the quotient T/N_e appearing in the Debye radius. With all this in mind, a simulation process results as being characterized by the value $\rho \equiv R_0/R_D$, $R_D = \sqrt{\epsilon_0 kT/q_e^2 N_e}$, the Debye radius. The significance of this characterization is that once a value has been fixed for ρ, the same numerical generation process of the temporal sequence of electric microfield of any species can be used for any pair (N_e, T) as soon as the following relation holds between N_e and T:

$$\frac{N_e^{1/6}}{T^{1/2}} = \left(\frac{4\pi}{3}\right)^{1/3} \left(\frac{\epsilon_0 k}{q^2}\right)^{1/2} \rho. \tag{7}$$

This allows a superior re-usability of the calculation of this microfield temporal sequence which, in our case, represents the highest amount of computer time involved in a simulation process. The *natural* time scale is different for ions and electrons and, in the former, the value of the reduced mass μ of the emitter–perturber pair should also be taken into account. To handle this variability, while trying to keep the highest reusability level, the following procedure has been applied.

(i) A value of ρ is fixed, which determines a set of useful (N_e, T) pairs. A temporal

sequence of the electric microfield of the electrons is obtained. The length of this sequence will be determined by the least advantageous of the conditions of these pairs, in terms of the calculation of the autocorrelation of the atomic dipole momentum. This is the first stage for reusability.

A small enough value of the discrete time step $\Delta\tau$ is chosen in order to get an adequate resolution of the time variations of the electric microfield. The value imposed by this condition is much smaller than the one demanded by the requirement of a good numerical accuracy in the numerical integration of the differential equations involved in the process [17]. In all the simulations carried out in this work, a value $\Delta\tau = 0.01$ was used, measured in simulation units. This means that a typical completed collision is tracked by 200 simulation time steps, which is more than enough if one takes into account the shape of the electric field as a function of time in a pair collision process.

(ii) The time sequence of the ion microfield is then simulated. Since we are dealing with independent particles from the cinematic point of view, this calculation process is completely independent of the previous one. As with the electrons, a time step $\Delta\tau = 0.01$ was chosen in all cases. However, since the natural time scale of the ions is different and depends on the value of μ, the two time sequences will not be isochronous. In order to obtain the total electric field acting on the emitter at a given time an interpolation must be carried out in the ion-microfield sequence before we can add its contribution to that of the electrons. This interpolation process obviously depends on the reduced mass value under consideration. In consequence, the same calculation of the ionic microfield can be useful for several μ values. This is the second stage for reusability.

(iii) Once the values for ρ and μ are fixed, all the necessary information is at hand to generate the microfield time sequences of ions and electrons and to properly overlap them. Then, a sequence of N_e values is run where every N_e has its corresponding T value: the one given by the ρ relation. For every (N_e, T) pair, the set of differential equations which give the time evolution of the autocorrelation function can be integrated and this can be finally computed using the technique described below (see section 2.4).

2.2. Statistical bias of the initial conditions

In previous works [13, 14, 17] a histogram was used in order to bias the probability density function of the ion electric-field modulus at $t = 0$ so that it corresponds with a Hooper's distribution [29]. This step was a consequence of the low number of simulation runs that made up the computation of every line profile. The number of runs in this work is noticeable higher and this statistical weighting is not necessary since Hooper's distribution naturally arises when the number of runs grows to infinity. Nevertheless, the validity of this decision has been carefully checked and a histogram of the initial values of the ionic field has been recorded to this end. With cells of width 7/100 (in Holtsmark field units) for electric fields between 0 and 7 units, the mean square deviation of the recorded histogram from the theoretical value was below 10% for a full simulation process comprising 5000 runs. This deviation was below 9% when the whole set of 15 000 or 20 000 runs was considered. Obviously these are worse-case referential values, since the standard deviation is drastically lowered when a more reasonable and wider field-cell value is used.

2.3. Solving the evolution equations

The numerical solution of equation (3) has been carried out in terms of the Euler–Rodrigues parameters, following the lines of [28], which will be briefly summarized here.

When the transition $n \to n'$ between levels with principal quantum numbers n and n' is to be studied, the *no-quenching* approximation yields a rewriting of equation (3) of the form

$$i\hbar \frac{d}{dt} \begin{pmatrix} U_n(t) & 0 \\ 0 & U_{n'}(t) \end{pmatrix} = q\boldsymbol{E}(t) \cdot \begin{pmatrix} \boldsymbol{R}_n & 0 \\ 0 & \boldsymbol{R}_{n'} \end{pmatrix} \begin{pmatrix} U_n(t) & 0 \\ 0 & U_{n'}(t) \end{pmatrix}, \tag{8}$$

so that for every group of states of principal quantum number n

$$i\hbar \frac{d}{dt} U_n(t) = q\boldsymbol{E}(t) \cdot \boldsymbol{R}_n U_n(t). \tag{9}$$

In hydrogenic atoms, the restriction of the position operator to the group of states of principal quantum number n, $\boldsymbol{R}_n$ can be written in terms of the Runge–Lenz operator $\boldsymbol{M}_n$ [30]

$$\boldsymbol{R}_n = -\tfrac{3}{2} n a_0 \boldsymbol{M}_n, \tag{10}$$

where a_0 is the Bohr radius. Together, the Runge–Lenz operator and the angular momentum operator $\boldsymbol{L}_n$ are the generators of an $SO(4)$ group which can be expressed as a direct sum of two $SO(3)$ groups, generated by two commuting infinitesimal generators

$$\boldsymbol{J}_n(1) = \frac{1}{2\hbar}(\boldsymbol{L}_n + \boldsymbol{M}_n),$$
$$\boldsymbol{J}_n(2) = \frac{1}{2\hbar}(\boldsymbol{L}_n - \boldsymbol{M}_n). \tag{11}$$

This fact allows the decoupling of differential equation (9) into two separated equations for the functions $\Phi_{n1}(t)$ and $\Phi_{n2}(t)$, defined by the expression

$$U_n(t) = \Phi_{n1}(t)\Phi_{n2}(t), \tag{12}$$

so that

$$i\frac{d}{dt}\Phi_{nk}(t) = \chi_{nk}\boldsymbol{E}(t) \cdot \boldsymbol{J}_n(k)\Phi_{nk}(t) \tag{13}$$

$$\chi_{nk} = (-1)^k \frac{3}{2\hbar} n q a_0, \qquad k = 1, 2. \tag{14}$$

Each of the two solutions of (13) is a rotation matrix of the form

$$\Phi_{nk}(t) = \exp[-i\psi_{nk}\boldsymbol{u}_{nk}(t) \cdot \boldsymbol{J}(k)], \tag{15}$$

with $|\boldsymbol{u}_{nk}| = 1$. This rotation can be expressed in terms of the Euler–Rodrigues parameters [31]:

$$\alpha_{nk}^0 = \cos(\tfrac{1}{2}\psi_{nk})$$
$$\boldsymbol{\alpha}_{nk} = \boldsymbol{u}_{nk}\sin(\tfrac{1}{2}\psi_{nk}), \tag{16}$$

and equations (13) may be written in terms of these parameters as

$$\frac{d}{dt}\alpha_{nk}^0 = -\boldsymbol{G}_{nk} \cdot \boldsymbol{\alpha}_{nk},$$
$$\frac{d}{dt}\boldsymbol{\alpha}_{nk} = \alpha_{nk}^0 \boldsymbol{G}_{nk} + \boldsymbol{G}_{nk} \times \boldsymbol{\alpha}_{nk}, \tag{17}$$

where $\boldsymbol{G}_{nk}(t) = \tfrac{1}{2}\chi_{nk}\boldsymbol{E}(t)$. These equations can be rewritten in a more compact form if quaternions are used:

$$\frac{d}{dt}\alpha_{nk} = G_{nk}(t)\alpha_{nk}, \tag{18}$$

with $\alpha \equiv [\![\alpha^0; \boldsymbol{\alpha}]\!]$ and $G \equiv [\![0; \boldsymbol{G}]\!]$ two quaternions whose product rules are shown in expressions (17). Now, the subindices nk will be omitted for easier writing.

When quaternion G is constant—that is to say, $\boldsymbol{E}$ does not depend on time—the solution of (18) will be

$$\alpha(t) = [\![\cos(|\boldsymbol{G}|t); \sin(|\boldsymbol{G}|t)\boldsymbol{u}_G]\!], \qquad \boldsymbol{u}_G = \frac{\boldsymbol{G}}{|\boldsymbol{G}|}. \tag{19}$$

The time step used in our simulations is small enough to assume that the electric field is constant within that time interval. So, the following operator may be taken as a solution of (18) at time $t_j = j\Delta t$:

$$\alpha(t_j) = [\![\cos(|\boldsymbol{G}_j|\Delta t); \sin(|\boldsymbol{G}_j|\Delta t)\boldsymbol{u}_{G_j}]\!]\alpha(t_{j-1}), \tag{20}$$

where $\boldsymbol{G}_j = \boldsymbol{G}(t_j)$ and $\alpha(0) = [\![1; \boldsymbol{0}]\!]$. This solution has a number of advantages: it is simple, it gives enough precision—better than a numerical counterpart obtained by a traditional Runge–Kutta with the same time step—numerical stability is guaranteed since the quaternion that converts the solution at time t_j into the one at time t_{j+1} has unit norm, which will be true for all times since the quaternion at $t = 0$ is also unitary. In a real simulation, this stability property will only be affected by the rounding error and even in this case this will be an arbitrary sign error which will not be thus amplified along the simulation process. Tests showed that, in all cases, the stability condition for the unitary character of the quaternion was preserved within the least significant decimal digit of the computer.

The instantaneous solution of equation (18) is determined by the electric-field direction $\boldsymbol{u}_G$ and modulus G, which value is

$$|\boldsymbol{G}_n|\Delta t = \frac{3}{4\hbar}nqa_0|\boldsymbol{E}|\Delta t = \frac{3}{4}n\hbar\frac{1}{m_e R_0 v_0}|\boldsymbol{F}|\Delta\tau$$

$$= n\hbar\left(\frac{9\pi}{16}\right)^{\frac{1}{3}}\left(\frac{1}{2m_e k}\right)^{\frac{1}{2}}N_e^{\frac{1}{3}}T^{-\frac{1}{2}}|\boldsymbol{F}|\Delta\tau$$

$$= 2.542 \times 10^{-8}nN_e^{\frac{1}{3}}T^{-\frac{1}{2}}|\boldsymbol{F}|\Delta\tau \qquad (MKS), \tag{21}$$

where $\boldsymbol{F}$ represents the electric field in simulation units—its value will then be around 1— and $\Delta\tau$ is the simulation time step—0.01 in all cases. In a typical situation $N_e = 10^{23}$ m^{-3}, $T = 10^4$ K, the argument of the trigonometric functions in (20) will be 2.4×10^{-4} for the quantum level $n = 2$.

2.4. Calculation of the autocorrelation function

The autocorrelation function may be obtained from expression (2). The total evolution operator has, in boxes, the structure given by (8). On the other hand, the dipole transition matrix has the form

$$D = \begin{pmatrix} 0 & \boldsymbol{d} \\ \boldsymbol{d}^+ & 0 \end{pmatrix}. \tag{22}$$

Bringing this expression to (2) yields

$$C(t) = \mathrm{tr}\begin{pmatrix} \boldsymbol{d} \cdot U_{n'}^+\boldsymbol{d}^+U_n & 0 \\ 0 & \boldsymbol{d}^+ \cdot U_n^+\boldsymbol{d}U_{n'} \end{pmatrix}$$

$$= \mathrm{tr}(\boldsymbol{d} \cdot U_{n'}^+\boldsymbol{d}^+U_n) + \mathrm{tr}(\boldsymbol{d}^+ \cdot U_n^+\boldsymbol{d}U_{n'})$$

$$= 2\,\mathrm{Re}\,\mathrm{tr}(\boldsymbol{d}^+ \cdot U_n^+\boldsymbol{d}U_{n'}). \tag{23}$$

The evolution operators of each level have the form given by (12) and (15):

$$U_n(t) = \exp[-i\psi_{n1}(t)u_{n1}(t) \cdot J_n(1)] \exp[-i\psi_{n2}(t)u_{n2}(t) \cdot J_n(2)]. \qquad (24)$$

The operators $J_n(1)$ and $J_n(2)$ are angular momentum operators with $j_n = (n-1)/2$ [32].

To give an expression of the autocorrelation function in terms of the Euler–Rodrigues parameters, it is necessary to expand the matrices of the evolution operators in powers of the matrices $\psi(t)u(t) \cdot J$. The eigenvalues equation of the latter limits the infinite series expansion of the exponential of the matrix to a polynomial of finite degree. If the nk indices from the argument of the exponential are dropped for ease of writing, the following equation will be obtained for any of the four cases

$$\Phi_n(t) = \exp[-i\psi(t)u(t) \cdot J]$$
$$= \sum_{k=0}^{n-1} f_k(\psi)(u \cdot J)^k. \qquad (25)$$

The upper limit for k in this sum is fixed by the degree of the eigenvalues equation for $(u \cdot J)$. Since this operator has $2j_n + 1 = n$ eigenvalues, the characteristic equation will give the dependence of $(u \cdot J)^n$ on its smaller powers.

A more convenient form of (25) will be

$$\Phi_n(t) = \sum_{k=0}^{n-1} [-i]_k P_k(\alpha_0)(\alpha \cdot J)^k, \qquad (26)$$

where we let $[-i]_k = 1$ for k zero or even and $[-i]_k = -i$ for odd values of k. The quantities (α_0, α) are the group of Euler–Rodrigues parameters. The functions $P_k(\alpha_0)$ are the unknowns of the expressions. This alternative form of the evolution operator will soon be justified.

The expansion (26) does not depend on the orientation of vector u nor on the representation base chosen for the matrices. Thus, the base in which operator $u \cdot J$ is diagonal will be preferred since this yields to a relation among diagonal matrices. For every eigenvalue,

$$\exp[-i\psi J_m] = \cos(J_m\psi) - i\sin(J_m\psi)$$
$$= \sum_{k=0}^{n-1} [-i]_k P_k(\alpha_0)(J_m\alpha)^k, \qquad (27)$$

with $\alpha = \sin(\psi/2)$. Eigenvalues of $u \cdot J$ are integer or half-integer numbers. If the angle $\theta = \psi/2$ is used instead of ψ, the quantities $J_m\psi$ will be an integer number of times θ. For example, $J_m\psi = \{\pm 4, \pm 2, 0\}\theta$ for $n = 5$ and $J_m\psi = \{\pm 3, \pm 1\}\theta$ for $n = 4$.

Real and imaginary parts can be separated in the relations (27) to get

$$\cos(2J_m\theta) = \sum_{k \text{ even}}^{n-1} P_k(\alpha_0)(J_m\alpha)^k, \qquad (28)$$

$$\sin(2J_m\theta) = \sum_{k \text{ odd}}^{n-1} P_k(\alpha_0)(J_m\alpha)^k. \qquad (29)$$

Relations (28) and (29) can be transformed into a system of linear equations. This can be done starting with the well known expansions

$$\cos m\theta = T_m(\cos\theta) = T_m(\alpha_0), \qquad (30)$$
$$\sin(m+1)\theta = \sin\theta\, U_m(\cos\theta) = \alpha Q_m(\alpha_0), \qquad (31)$$

Table 1. Plasma temperature in K for the conditions reflected in the simulations.

log N_e (m^{-3})	ρ									
	0.1	0.2	0.3	0.4	0.5	0.6	0.7	0.8	0.9	1.0
20.00	37 508	9 377	4 168	—	—	—	—	—	—	—
20.33	48 444	12 111	5 383	—	—	—	—	—	—	—
20.67	62 568	15 642	6 952	3 910	—	—	—	—	—	—
21.00	80 809	20 202	8 979	5 051	3 232	2245	—	—	—	—
21.33	104 369	26 092	11 597	6 523	4 175	2899	—	—	—	—
21.67	134 798	33 699	14 978	8 425	5 392	3 744	—	—	—	—
22.00	174 098	43 525	19 344	10 881	6 964	4 836	3 553	—	—	—
22.33	224 856	56 214	24 984	14 054	8 994	6 246	4 589	—	—	—
22.67	—	72 603	32 268	18 151	11 617	8 067	5 927	4 538	—	—
23.00	—	—	41 676	23 443	15 003	10 419	7 655	5 861	4 631	—
23.33	—	—	53 826	30 277	19 378	13 457	9 886	7 569	5 981	4 844
23.67	—	—	69 520	39 106	25 027	17 380	12 769	9 776	7 724	6 257
24.00	—	—	—	50 506	32 324	22 447	16 492	12 626	9 976	8 081
24.33	—	—	—	—	41 748	28 991	21 300	16 308	12 885	10 437
24.67	—	—	—	—	53 919	37 444	27 510	21 062	16 642	13 480

Table 2. Working conditions of the simulations: N_p, number of electrons; log N_e, range of simulated electron densities (in m^{-3}) in increments of $\frac{1}{3}$ of a decade. The two mentioned cases are included.

ρ	Series 1			Series 2		
	N_p	Samples	log N_e	N_p	Samples	log N_e
0.1	—	—	—	100	11 300	20.0–22.3
0.2	100	6 187	21.0–22.7	100	3×5000	20.0–22.7
0.2	500	7 010	21.0–22.7			
0.2	2700	5 121	22.0–22.7			
0.3	100	7 805	21.0–22.7	100	3 × 5000	20.0–23.7
0.4	100	7 686	21.0–23.7	100	4 × 5000	20.7–24.0
0.5	100	8 444	21.0–24.7	100	4 × 5000	21.0–24.7
0.6	100	7 482	21.0–24.7	100	4 × 5000	21.0–24.7
0.7	100	13 073	22.0–24.7	100	4 × 5000	22.0–24.7
0.8	100	7 388	23.0–24.7	100	4 × 5000	22.7–24.7
0.9	100	10 006	23.0–24.7	100	4 × 5000	23.0–24.7
1.0	100	10 002	24.0–24.7	100	4 × 5000	23.3–24.7

where $T_m(x)$ and $Q_m(x)$ are Chebyshev polynomials of degree m of the first and second order [33]. When these relations are used in (28) and (29) it is readily seen that all the terms in which the value α appears can be substituted by powers of α_0. Although (29) shows an expansion in odd powers of α, the substitution of $\sin(2J_m\theta)$ by $\alpha Q_{2J_m-1}(\alpha_0)$ allows the elimination of an α factor after which just the even powers remain. A final substitution of α^2 by $1 - \alpha_0^2$ will give relations in which only powers of α_0 appear. This clearly shows that the functions $P_k(\alpha_0)$ are polynomials in α_0. In particular,

$$T_{2J_m}(\alpha_0) = \sum_{k \text{ even}}^{n-1} P_k(\alpha_0) J_m^k (1 - \alpha_0^2)^{k/2}, \qquad (32)$$

Table 3. Lyman-α FWHM: comparison with the experimental results of Grützmacher and Wende [38], the simulations of Hegerfeld and Kesting [18] and semianalytical calculations by Oza *et al* [25]. $\mu = 0.975$. The Doppler effect has not been included.

N_e	T	$\Delta\lambda_{1/2}$ (nm)			
(10^{23} m^{-3})	(K)	This work	Reference [38]	Reference [18]	Reference [25][a]
1	12 700	0.0173	0.0175	0.015	0.0108
2	13 200	0.0258	0.0255	0.023	
3	13 200	0.0326	0.0320	0.031	
4	14 000	0.0389	0.0363	0.039	

[a] $T = 10\,000$ K.

Table 4. Balmer-α FWHM: comparison of the simulation results with the experimental data of several authors.

Plasma	N_e (m^{-3})	T (K)	FWHM (nm)		
			This work		Reference
H + Ar$^+$	5×10^{22}	12 500	0.658	0.62	[41]
H + Ar$^+$	8.5×10^{22}	12 500	0.913	0.80	[41]
H + Ar$^+$	10^{23}	12 500	1.010	0.91	[41]
H + He$^+$	4×10^{22}	30 000	0.665	0.75	[42]
H + He$^+$	4.5×10^{23}	30 000	2.94	3.61	[42]
H + He$^+$	10^{23}	31 000	1.16	1.26	[7]
H + He$^+$	2×10^{23}	29 500	1.75	1.75	[7]
H + He$^+$	2.8×10^{23}	26 000	2.14	2.16	[7]
H + Ar$^+$	1.4×10^{22}	9 600	0.298	0.30	[43]
D + Ar$^+$	1.4×10^{22}	9 600	0.263	0.26	[43]
H + He$^+$	1.4×10^{20}	20 000	0.016	0.033	[44]
H + Ar$^+$	6.1×10^{23}	16 000	3.47	3.2	[45]
H + Ar$^+$	6.2×10^{23}	17 400	3.52	3.5	[45]
H + Ar$^+$	7.4×10^{23}	17 700	3.98	3.7	[45]
H + Ar$^+$	8.2×10^{23}	18 000	4.28	3.9	[45]
H + Ar$^+$	9.4×10^{23}	18 500	4.71	4.1	[45]
H + Ar$^+$	10^{24}	18 700	4.92	4.4	[45]

$$Q_{2J_m-1}(\alpha_0) = \sum_{k \text{ odd}}^{n-1} P_k(\alpha_0) J_m^k (1 - \alpha_0^2)^{(k-1)/2}. \tag{33}$$

Taking the case $n = 5$ as an example, J_m would have the values $0, 1, 2$ so that the set of equations for that level would be

$$
\begin{aligned}
P_0 &= T_0(\alpha_0) \\
P_1 + (1 - \alpha_0^2)P_3 &= Q_1(\alpha_0) \\
P_0 + (1 - \alpha_0^2)P_2 + (1 - \alpha_0^2)^2 P_4 &= T_2(\alpha_0) \\
2P_1 + 8(1 - \alpha_0^2)P_3 &= Q_3(\alpha_0) \\
P_0 + 4(1 - \alpha_0^2)P_2 + 16(1 - \alpha_0^2)^2 P_4 &= T_4(\alpha_0)
\end{aligned}
\tag{34}
$$

Table 5. FWHM of Lyman-α (in nm). $\mu = 0.5$.

$\log(N_e)$ (m^{-3})	Temperature (K)					
	5000	10 000	15 000	20 000	30 000	40 000
21.00	1.27 (−3)	1.26 (−3)	1.21 (−3)	1.16 (−3)	—	—
21.33	2.10 (−3)	2.16 (−3)	2.14 (−3)	2.10 (−3)	1.99 (−3)	—
21.67	3.32 (−3)	3.55 (−3)	3.62 (−3)	3.62 (−3)	3.57 (−3)	—
22.00	5.08 (−3)	5.73 (−3)	5.98 (−3)	6.07 (−3)	6.08 (−3)	5.97 (−3)
22.33	7.57 (−3)	8.83 (−3)	9.42 (−3)	9.75 (−3)	1.01 (−2)	1.02 (−2)
22.67	1.11 (−2)	1.34 (−2)	1.46 (−2)	1.53 (−2)	—	—
23.00	1.77 (−2)	2.00 (−2)	2.18 (−2)	2.33 (−2)	—	—
23.33	2.82 (−2)	3.02 (−2)	3.24 (−2)	3.45 (−2)	3.86 (−2)	—
23.67	4.68 (−2)	4.77 (−2)	4.98 (−2)	5.23 (−2)	5.75 (−2)	6.26 (−2)
24.00	—	7.59 (−2)	7.92 (−2)	8.23 (−2)	8.82 (−2)	—
24.33	—	1.26 (−1)	1.28 (−1)	1.31 (−1)	1.37 (−1)	1.43 (−1)
24.67	—	—	2.15 (−1)	2.15 (−1)	2.20 (−1)	2.27 (−1)

The notation '1.27 (−3)' has been used to represent 1.27×10^{-3}.

Table 6. FWHM of Lyman-α (in nm). $\mu = 0.8$.

$\log(N_e)$ (m^{-3})	Temperature (K)					
	5000	10 000	15 000	20 000	30 000	40 000
21.00	1.23 (−3)	1.27 (−3)	1.27 (−3)	1.25 (−3)	—	—
21.33	1.97 (−3)	2.12 (−3)	2.16 (−3)	2.17 (−3)	2.14 (−3)	—
21.67	3.00 (−3)	3.38 (−3)	3.54 (−3)	3.62 (−3)	3.67 (−3)	—
22.00	4.49 (−3)	5.22 (−3)	5.59 (−3)	5.81 (−3)	6.05 (−3)	6.18 (−3)
22.33	6.53 (−3)	7.97 (−3)	8.71 (−3)	9.16 (−3)	9.70 (−3)	9.99 (−3)
22.67	9.53 (−3)	1.18 (−2)	1.30 (−2)	1.38 (−2)	—	—
23.00	1.56 (−2)	1.73 (−2)	1.91 (−2)	2.08 (−2)	—	—
23.33	2.48 (−2)	2.70 (−2)	2.89 (−2)	3.06 (−2)	3.36 (−2)	—
23.67	4.13 (−2)	4.30 (−2)	4.49 (−2)	4.67 (−2)	5.01 (−2)	5.32 (−2)
24.00	—	7.01 (−2)	7.12 (−2)	7.33 (−2)	7.84 (−2)	—
24.33	—	1.19 (−1)	1.19 (−1)	1.20 (−1)	1.24 (−1)	1.29 (−1)
24.67	—	—	2.01 (−1)	2.03 (−1)	2.06 (−1)	2.09 (−1)

The notation '1.27 (−3)' has been used to represent 1.27×10^{-3}.

Then, for $n = 5$, we have

$$
\begin{aligned}
P_0(\alpha_0) &= 1, \\
P_1(\alpha_0) &= \tfrac{4}{3}Q_1 - \tfrac{1}{6}Q_3 = -\tfrac{4}{3}\alpha_0^3 - 2\alpha_0, \\
P_2(\alpha_0) &= \frac{1}{1 - \alpha_0^2}[-\tfrac{5}{4}T_0 + \tfrac{4}{3}T_2 - \tfrac{1}{12}T_4] = \tfrac{2}{3}[\alpha_0^2 - 4], \\
P_3(\alpha_0) &= \frac{1}{1 - \alpha_0^2}[-\tfrac{1}{3}Q_1 + \tfrac{1}{6}Q_3] = -\tfrac{4}{3}\alpha_0, \\
P_4(\alpha_0) &= \frac{1}{(1 - \alpha_0^2)^2}[-\tfrac{1}{4}T_0 - \tfrac{1}{3}T_2 + \tfrac{1}{12}T_4] = \tfrac{2}{3}.
\end{aligned}
\tag{35}
$$

Which finally yields

$$
\Phi_5(t) = \exp[-i\psi \boldsymbol{u} \cdot \boldsymbol{J}] = \mathbb{I} + \tfrac{2}{3}i\alpha_0(2\alpha_0^2 - 3)(\boldsymbol{\alpha} \cdot \boldsymbol{J}) + \tfrac{2}{3}(\alpha_0^2 - 4)(\boldsymbol{\alpha} \cdot \boldsymbol{J})^2
$$

Table 7. FWHM of Lyman-α (in nm). $\mu = 0.9$.

$\log(N_e)$ (m^{-3})	Temperature (K)					
	5000	10 000	15 000	20 000	30 000	40 000
21.00	1.22 (−3)	1.28 (−3)	1.28 (−3)	1.27 (−3)	—	—
21.33	1.92 (−3)	2.09 (−3)	2.15 (−3)	2.18 (−3)	2.19 (−3)	—
21.67	2.91 (−3)	3.30 (−3)	3.48 (−3)	3.58 (−3)	3.67 (−3)	—
22.00	4.33 (−3)	5.09 (−3)	5.47 (−3)	5.71 (−3)	5.99 (−3)	6.15 (−3)
22.33	6.31 (−3)	7.69 (−3)	8.41 (−3)	8.88 (−3)	9.45 (−3)	9.79 (−3)
22.67	9.34 (−3)	1.14 (−2)	1.26 (−2)	1.34 (−2)	—	—
23.00	1.53 (−2)	1.69 (−2)	1.84 (−2)	1.99 (−2)	—	—
23.33	2.43 (−2)	2.62 (−2)	2.79 (−2)	2.94 (−2)	3.21 (−2)	—
23.67	4.00 (−2)	4.20 (−2)	4.38 (−2)	4.54 (−2)	4.84 (−2)	5.10 (−2)
24.00	—	6.90 (−2)	6.97 (−2)	7.15 (−2)	7.63 (−2)	—
24.33	—	1.17 (−1)	1.17 (−1)	1.19 (−1)	1.21 (−1)	1.24 (−1)
24.67	—	—	1.99 (−1)	2.01 (−1)	2.03 (−1)	2.05 (−1)

The notation '1.27 (−3)' has been used to represent 1.27×10^{-3}.

Table 8. FWHM of Lyman-α (in nm). $\mu = 1$.

$\log(N_e)$ (m^{-3})	Temperature (K)					
	5000	10 000	15 000	20 000	30 000	40 000
21.00	1.21 (−3)	1.28 (−3)	1.30 (−3)	1.29 (−3)	—	—
21.33	1.87 (−3)	2.06 (−3)	2.14 (−3)	2.18 (−3)	2.22 (−3)	—
21.67	2.85 (−3)	3.25 (−3)	3.44 (−3)	3.55 (−3)	3.68 (−3)	—
22.00	4.21 (−3)	5.00 (−3)	5.40 (−3)	5.64 (−3)	5.92 (−3)	6.07 (−3)
22.33	6.07 (−3)	7.48 (−3)	8.22 (−3)	8.70 (−3)	9.29 (−3)	9.64 (−3)
22.67	9.10 (−3)	1.11 (−2)	1.22 (−2)	1.30 (−2)	—	—
23.00	1.48 (−2)	1.64 (−2)	1.79 (−2)	1.93 (−2)	—	—
23.33	2.44 (−2)	2.58 (−2)	2.73 (−2)	2.87 (−2)	3.13 (−2)	—
23.67	3.89 (−2)	4.08 (−2)	4.25 (−2)	4.43 (−2)	4.74 (−2)	5.03 (−2)
24.00	—	6.79 (−2)	6.84 (−2)	6.98 (−2)	7.40 (−2)	—
24.33	—	1.16 (−1)	1.16 (−1)	1.17 (−1)	1.19 (−1)	1.22 (−1)
24.67	—	—	1.96 (−1)	1.98 (−1)	2.00 (−1)	2.01 (−1)

The notation '1.27 (−3)' has been used to represent 1.27×10^{-3}.

$$+ \tfrac{2}{3} i 2 \alpha_0 (\boldsymbol{\alpha} \cdot \boldsymbol{J})^3 + \tfrac{2}{3} (\boldsymbol{\alpha} \cdot \boldsymbol{J})^4. \tag{36}$$

With a similar procedure, all the Φ_{nk} may be expressed as polynomials in Euler–Rodrigues parameters. At the same time, the matrices $\boldsymbol{J}_n(k)$ can be written as a function of the operators $\boldsymbol{R}_n$ and $\boldsymbol{L}_n$ using the definitions (11). The explicit form of these operators can be found in [34].

As a consequence of the trace of the product of these matrices which appears in (23), the autocorrelation function can be written as a polynomial in the four groups of Euler–Rodrigues parameters, two for each of the two levels of a transition. This calculation can be carried out with the help of some symbolic calculation tool. The final expressions of the autocorrelation functions of the lines calculated in this work appear elsewhere (see [28, 17, 19] and also the appendix of this paper for the Lyman-γ line).

Table 9. FWHM of Lyman-α (in nm). $\mu = 2$.

log(N_e) (m⁻³)	Temperature (K)					
	5000	10 000	15 000	20 000	30 000	40 000
21.00	1.09 (−3)	1.23 (−3)	1.28 (−3)	1.30 (−3)	—	—
21.33	1.61 (−3)	1.87 (−3)	2.00 (−3)	2.08 (−3)	2.16 (−3)	—
21.67	2.35 (−3)	2.83 (−3)	3.08 (−3)	3.24 (−3)	3.44 (−3)	—
22.00	3.40 (−3)	4.11 (−3)	4.53 (−3)	4.83 (−3)	5.26 (−3)	5.58 (−3)
22.33	4.97 (−3)	5.97 (−3)	6.60 (−3)	7.07 (−3)	7.78 (−3)	8.33 (−3)
22.67	7.69 (−3)	8.86 (−3)	9.66 (−3)	1.03 (−2)	—	—
23.00	1.28 (−2)	1.37 (−2)	1.46 (−2)	1.55 (−2)	—	—
23.33	2.12 (−2)	2.20 (−2)	2.28 (−2)	2.37 (−2)	2.54 (−2)	—
23.67	3.64 (−2)	3.62 (−2)	3.67 (−2)	3.75 (−2)	3.92 (−2)	4.09 (−2)
24.00	—	6.15 (−2)	6.12 (−2)	6.16 (−2)	6.31 (−2)	—
24.33	—	1.05 (−1)	1.08 (−1)	1.08 (−1)	1.06 (−1)	1.03 (−1)
24.67	—	—	1.86 (−1)	1.85 (−1)	1.83 (−1)	1.80 (−1)

The notation '1.27 (−3)' has been used to represent 1.27×10^{-3}.

Table 10. FWHM of Lyman-β (in nm). $\mu = 0.5$.

log(N_e) (m⁻³)	Temperature (K)					
	5000	10 000	15 000	20 000	30 000	40 000
20.00	1.12 (−3)	1.03 (−3)	9.62 (−4)	9.12 (−4)	8.33 (−4)	7.70 (−4)
20.33	1.97 (−3)	1.84 (−3)	1.74 (−3)	1.67 (−3)	1.55 (−3)	1.46 (−3)
20.67	3.46 (−3)	3.35 (−3)	3.24 (−3)	3.13 (−3)	2.94 (−3)	2.77 (−3)
21.00	5.97 (−3)	5.98 (−3)	5.87 (−3)	5.74 (−3)	5.45 (−3)	5.17 (−3)
21.33	1.00 (−2)	1.03 (−2)	1.02 (−2)	1.01 (−2)	9.82 (−3)	9.48 (−3)
21.67	1.68 (−2)	1.74 (−2)	1.76 (−2)	1.75 (−2)	1.73 (−2)	1.69 (−2)
22.00	2.77 (−2)	2.92 (−2)	2.97 (−2)	2.99 (−2)	2.98 (−2)	2.95 (−2)
22.33	4.57 (−2)	4.84 (−2)	4.96 (−2)	5.01 (−2)	5.05 (−2)	5.05 (−2)
22.67	7.50 (−2)	8.03 (−2)	8.27 (−2)	8.40 (−2)	8.51 (−2)	8.53 (−2)
23.00	1.23 (−1)	1.34 (−1)	1.39 (−1)	1.41 (−1)	1.43 (−1)	1.42 (−1)
23.33	1.99 (−1)	2.21 (−1)	2.31 (−1)	2.36 (−1)	2.39 (−1)	2.39 (−1)
23.67	3.19 (−1)	3.60 (−1)	3.81 (−1)	3.92 (−1)	4.03 (−1)	4.06 (−1)
24.00	—	5.89 (−1)	6.29 (−1)	6.52 (−1)	6.70 (−1)	6.72 (−1)
24.33	—	9.44 (−1)	1.03 (+0)	1.07 (+0)	1.12 (+0)	1.13 (+0)
24.67	—	—	1.65 (+0)	1.76 (+0)	1.88 (+0)	1.93 (+0)

The notation '1.27 (−3)' has been used to represent 1.27×10^{-3}.

3. Broadening regimes of the ion dynamics effects

To analyse the functional behaviour of the width of the spectral lines in terms of the density, temperature and reduced mass μ, it is good practice to have a look at the effect of an individual collision. When the electric field which perturbs the emitter is caused by a single particle under linear and uniform motion, the equations (17) can be solved analytically [35, 36]. If, in a further approximation, the collision is considered to be complete, the

Table 11. FWHM of Lyman-β (in nm). $\mu = 0.8$.

log(N_e) (m^{-3})	Temperature (K)					
	5000	10 000	15 000	20 000	30 000	40 000
20.00	1.19 (−3)	1.10 (−3)	1.04 (−3)	9.96 (−4)	9.21 (−4)	8.60 (−4)
20.33	2.11 (−3)	1.97 (−3)	1.87 (−3)	1.80 (−3)	1.68 (−3)	1.59 (−3)
20.67	3.58 (−3)	3.56 (−3)	3.49 (−3)	3.40 (−3)	3.22 (−3)	3.06 (−3)
21.00	6.02 (−3)	6.12 (−3)	6.07 (−3)	5.98 (−3)	5.77 (−3)	5.54 (−3)
21.33	1.01 (−2)	1.05 (−2)	1.06 (−2)	1.05 (−2)	1.03 (−2)	1.00 (−2)
21.67	1.68 (−2)	1.75 (−2)	1.78 (−2)	1.78 (−2)	1.76 (−2)	1.74 (−2)
22.00	2.75 (−2)	2.89 (−2)	2.95 (−2)	2.98 (−2)	2.99 (−2)	2.99 (−2)
22.33	4.51 (−2)	4.79 (−2)	4.92 (−2)	4.99 (−2)	5.05 (−2)	5.06 (−2)
22.67	7.38 (−2)	7.93 (−2)	8.18 (−2)	8.32 (−2)	8.46 (−2)	8.50 (−2)
23.00	1.21 (−1)	1.32 (−1)	1.37 (−1)	1.39 (−1)	1.40 (−1)	1.40 (−1)
23.33	1.96 (−1)	2.19 (−1)	2.29 (−1)	2.34 (−1)	2.38 (−1)	2.37 (−1)
23.67	3.21 (−1)	3.58 (−1)	3.76 (−1)	3.87 (−1)	3.98 (−1)	4.02 (−1)
24.00	—	5.89 (−1)	6.28 (−1)	6.49 (−1)	6.67 (−1)	6.69 (−1)
24.33	—	9.42 (−1)	1.03 (+0)	1.08 (+0)	1.12 (+0)	1.12 (+0)
24.67	—	—	1.65 (+0)	1.75 (+0)	1.87 (+0)	1.91 (+0)

The notation '1.27 (−3)' has been used to represent 1.27×10^{-3}.

Table 12. FWHM of Lyman-β (in nm). $\mu = 0.9$.

log(N_e) (m^{-3})	Temperature (K)					
	5000	10 000	15 000	20 000	30 000	40 000
20.00	1.21 (−3)	1.11 (−3)	1.05 (−3)	1.00 (−3)	9.28 (−4)	8.72 (−4)
20.33	2.15 (−3)	2.02 (−3)	1.94 (−3)	1.87 (−3)	1.76 (−3)	1.67 (−3)
20.67	3.61 (−3)	3.58 (−3)	3.50 (−3)	3.42 (−3)	3.25 (−3)	3.09 (−3)
21.00	6.05 (−3)	6.15 (−3)	6.12 (−3)	6.04 (−3)	5.85 (−3)	5.65 (−3)
21.33	1.01 (−2)	1.05 (−2)	1.06 (−2)	1.05 (−2)	1.03 (−2)	1.01 (−2)
21.67	1.67 (−2)	1.74 (−2)	1.77 (−2)	1.78 (−2)	1.77 (−2)	1.76 (−2)
22.00	2.74 (−2)	2.90 (−2)	2.96 (−2)	2.99 (−2)	3.01 (−2)	3.00 (−2)
22.33	4.50 (−2)	4.78 (−2)	4.91 (−2)	4.98 (−2)	5.04 (−2)	5.06 (−2)
22.67	7.38 (−2)	7.88 (−2)	8.12 (−2)	8.26 (−2)	8.41 (−2)	8.48 (−2)
23.00	1.21 (−1)	1.32 (−1)	1.37 (−1)	1.39 (−1)	1.40 (−1)	1.39 (−1)
23.33	1.96 (−1)	2.18 (−1)	2.28 (−1)	2.34 (−1)	2.37 (−1)	2.36 (−1)
23.67	3.21 (−1)	3.58 (−1)	3.76 (−1)	3.87 (−1)	3.97 (−1)	4.01 (−1)
24.00	—	5.88 (−1)	6.28 (−1)	6.49 (−1)	6.66 (−1)	6.66 (−1)
24.33	—	9.43 (−1)	1.02 (+0)	1.07 (+0)	1.11 (+0)	1.12 (+0)
24.67	—	—	1.65 (+0)	1.75 (+0)	1.87 (+0)	1.91 (+0)

The notation '1.27 (−3)' has been used to represent 1.27×10^{-3}.

Euler–Rodrigues parameters after the collision have the values (see [21]):

$$
\alpha_0 = \frac{1}{\sigma} \sin(\sigma\pi/2)
$$
$$
\boldsymbol{\alpha} = \frac{\delta}{\sigma} \sin(\sigma\pi/2)\boldsymbol{u}_b + \cos(\sigma\pi/2)\boldsymbol{u}_b \times \boldsymbol{u}_v,
$$
(37)

Table 13. FWHM of Lyman-β (in nm). $\mu = 1$.

$\log(N_e)$ (m^{-3})	Temperature (K)					
	5000	10 000	15 000	20 000	30 000	40 000
20.00	1.23 (−3)	1.13 (−3)	1.07 (−3)	1.02 (−3)	9.53 (−4)	8.97 (−4)
20.33	2.15 (−3)	2.04 (−3)	1.96 (−3)	1.89 (−3)	1.79 (−3)	1.71 (−3)
20.67	3.61 (−3)	3.59 (−3)	3.52 (−3)	3.44 (−3)	3.28 (−3)	3.12 (−3)
21.00	6.07 (−3)	6.22 (−3)	6.20 (−3)	6.12 (−3)	5.92 (−3)	5.71 (−3)
21.33	1.00 (−2)	1.04 (−2)	1.05 (−2)	1.05 (−2)	1.03 (−2)	1.01 (−2)
21.67	1.66 (−2)	1.74 (−2)	1.77 (−2)	1.78 (−2)	1.78 (−2)	1.76 (−2)
22.00	2.73 (−2)	2.90 (−2)	2.97 (−2)	3.00 (−2)	3.02 (−2)	3.02 (−2)
22.33	4.47 (−2)	4.77 (−2)	4.90 (−2)	4.98 (−2)	5.05 (−2)	5.07 (−2)
22.67	7.36 (−2)	7.88 (−2)	8.13 (−2)	8.27 (−2)	8.43 (−2)	8.49 (−2)
23.00	1.20 (−1)	1.32 (−1)	1.37 (−1)	1.39 (−1)	1.40 (−1)	1.39 (−1)
23.33	1.96 (−1)	2.18 (−1)	2.28 (−1)	2.33 (−1)	2.36 (−1)	2.36 (−1)
23.67	3.20 (−1)	3.57 (−1)	3.76 (−1)	3.86 (−1)	3.97 (−1)	4.00 (−1)
24.00	—	5.89 (−1)	6.27 (−1)	6.47 (−1)	6.65 (−1)	6.67 (−1)
24.33	—	9.43 (−1)	1.02 (+0)	1.07 (+0)	1.11 (+0)	1.12 (+0)
24.67	—	—	1.64 (+0)	1.75 (+0)	1.87 (+0)	1.91 (+0)

The notation '1.27 (−3)' has been used to represent 1.27×10^{-3}.

Table 14. FWHM of Lyman-β (in nm). $\mu = 2$.

$\log(N_e)$ (m^{-3})	Temperature (K)					
	5000	10 000	15 000	20 000	30 000	40 000
20.00	1.29 (−3)	1.24 (−3)	1.20 (−3)	1.16 (−3)	1.10 (−3)	1.05 (−3)
20.33	2.23 (−3)	2.17 (−3)	2.12 (−3)	2.07 (−3)	1.99 (−3)	1.91 (−3)
20.67	3.65 (−3)	3.74 (−3)	3.72 (−3)	3.68 (−3)	3.57 (−3)	3.45 (−3)
21.00	6.02 (−3)	6.26 (−3)	6.31 (−3)	6.30 (−3)	6.22 (−3)	6.10 (−3)
21.33	9.89 (−3)	1.04 (−2)	1.05 (−2)	1.06 (−2)	1.06 (−2)	1.05 (−2)
21.67	1.62 (−2)	1.70 (−2)	1.74 (−2)	1.76 (−2)	1.77 (−2)	1.77 (−2)
22.00	2.67 (−2)	2.82 (−2)	2.89 (−2)	2.93 (−2)	2.97 (−2)	2.99 (−2)
22.33	4.42 (−2)	4.68 (−2)	4.80 (−2)	4.88 (−2)	4.96 (−2)	5.00 (−2)
22.67	7.35 (−2)	7.80 (−2)	8.02 (−2)	8.14 (−2)	8.27 (−2)	8.31 (−2)
23.00	1.20 (−1)	1.31 (−1)	1.35 (−1)	1.37 (−1)	1.37 (−1)	1.35 (−1)
23.33	1.96 (−1)	2.17 (−1)	2.26 (−1)	2.30 (−1)	2.32 (−1)	2.30 (−1)
23.67	3.19 (−1)	3.56 (−1)	3.74 (−1)	3.84 (−1)	3.94 (−1)	3.96 (−1)
24.00	—	5.86 (−1)	6.22 (−1)	6.43 (−1)	6.62 (−1)	6.67 (−1)
24.33	—	9.36 (−1)	1.02 (+0)	1.07 (+0)	1.11 (+0)	1.11 (+0)
24.67	—	—	1.64 (+0)	1.75 (+0)	1.86 (+0)	1.91 (+0)

The notation '1.27 (−3)' has been used to represent 1.27×10^{-3}.

where $\boldsymbol{u}_b$ and $\boldsymbol{u}_v$ are the unit vectors along the impact parameter b and the velocity v of the perturber and

$$\sigma = \sqrt{1 + \delta^2}$$
$$\delta = \frac{3}{2} n a_0 \frac{q^2}{4\pi\epsilon_0\hbar} \frac{1}{bv},$$

(38)

with n the principal quantum number of the level. The parameter $\alpha_0 = \cos(\psi/2)$ accounts for the change in the phase ψ of the evolution operator. When this change is very small, even if the collision is indeed completed, we are faced with the impact-broadening mechanism.

Table 15. FWHM of Lyman-γ (in nm). $\mu = 0.5$.

log(N_e) (m^{-3})	Temperature (K)					
	5000	10 000	15 000	20 000	30 000	40 000
20.00	2.05 (−3)	2.04 (−3)	2.01 (−3)	1.98 (−3)	1.90 (−3)	1.84 (−3)
20.33	3.46 (−3)	3.47 (−3)	3.44 (−3)	3.40 (−3)	3.32 (−3)	3.24 (−3)
20.67	5.58 (−3)	5.83 (−3)	5.90 (−3)	5.90 (−3)	5.84 (−3)	5.74 (−3)
21.00	9.29 (−3)	9.86 (−3)	1.00 (−2)	1.01 (−2)	1.01 (−2)	9.93 (−3)
21.33	1.51 (−2)	1.63 (−2)	1.67 (−2)	1.69 (−2)	1.70 (−2)	1.70 (−2)
21.67	2.45 (−2)	2.65 (−2)	2.74 (−2)	2.79 (−2)	2.83 (−2)	2.85 (−2)
22.00	3.97 (−2)	4.30 (−2)	4.47 (−2)	4.56 (−2)	4.67 (−2)	4.72 (−2)
22.33	6.50 (−2)	7.06 (−2)	7.34 (−2)	7.51 (−2)	7.71 (−2)	7.82 (−2)
22.67	1.07 (−1)	1.16 (−1)	1.20 (−1)	1.23 (−1)	1.26 (−1)	1.28 (−1)
23.00	1.75 (−1)	1.91 (−1)	1.98 (−1)	2.03 (−1)	2.08 (−1)	2.11 (−1)
23.33	2.71 (−1)	3.13 (−1)	3.32 (−1)	3.42 (−1)	3.49 (−1)	3.49 (−1)
23.67	4.15 (−1)	4.98 (−1)	5.39 (−1)	5.63 (−1)	5.88 (−1)	5.97 (−1)
24.00	—	7.77 (−1)	8.55 (−1)	9.06 (−1)	9.69 (−1)	1.01 (+0)
24.33	—	1.21 (+0)	1.35 (+0)	1.44 (+0)	1.56 (+0)	1.63 (+0)
24.67	—	—	2.08 (+0)	2.26 (+0)	2.49 (+0)	2.62 (+0)

The notation '1.27 (−3)' has been used to represent 1.27×10^{-3}.

In those cases, the width of the line will be determined by the frequency of the collisions multiplied by that small phase change per collision. On the other hand, when ψ clearly exceeds the value π, the quasistatic field approximation applies. In the first case, if $\delta \ll 1$ then $\psi \approx 2\delta$. This means that the typical change in the evolution operator due to the collisions is $1 - U_n \sim 1 - \cos[(n-1)\psi/2] \approx (n-1)^2\delta^2/2$. If it is taken into account that this collision has a duration of the order of b/v, the width of the line will be given by

$$\delta \ll 1 \longrightarrow \Delta\lambda_{1/2} \sim \frac{\lambda_0^2}{2\pi c}\frac{1 - U_n}{\Delta t} \propto \delta^2\frac{v}{b} \propto \frac{N_e}{v}. \tag{39}$$

In other words, the impact width results in being linear in the electronic density and shows a dependence on the reduced mass and the temperature of the form $(\mu/T)^{1/2}$, as already known [25, 37]. As the value of δ grows—which happens when the electronic density diminishes or the temperature grows—the quantity $1 - \cos[(n-1)\psi/2]$ gets closer to 1 so that $(1-U_n)/\Delta t \approx (v/b)$. Specifically, when $\delta = \sqrt{3}$, the extreme case $\cos[(n-1)\psi/2] = 0$ is found. Then, as δ becomes bigger, the line width becomes proportional to v/b, which means that the dependence on the reduced mass and the temperature inverts.

When δ goes too far from unit value, the emission phase can change in several cycles along the duration of the collision, which means we are completely inside the validity domain of the quasistatic approximation, where the temperature dependence involves collective phenomenon and the individual collision model is no longer valid.

It is usually assumed that electronic collisions cause impact broadening in the range covered in the simulations presented here ($N_e = 10^{20} - 10^{24}$ m^{-3}; $T = 5000$–$40\,000$ K). The highest value, $\delta_e = 0.2$, corresponds to a Lyman-α line for the conditions $N_e = 4.6 \times 10^{24}$ m^{-3}, $T = 5000$ K. For the same line and with $\mu = 0.5$, $N_e = 10^{21}$ m^{-3}, and $T = 40\,000$ K, $\delta_i = 0.15$ for the ion collisions. In short, this means that a typical impact-broadening behaviour can be expected from the dynamic effects of the ions at the low density and high temperature situations of this work, as long as the dependence with the reduced mass and temperature are considered.

Table 16. FWHM of Lyman-γ (in nm). $\mu = 0.8$.

log(N_e) (m^{-3})	Temperature (K)					
	5000	10 000	15 000	20 000	30 000	40 000
20.00	2.04 (−3)	2.03 (−3)	2.02 (−3)	1.99 (−3)	1.95 (−3)	1.91 (−3)
20.33	3.36 (−3)	3.46 (−3)	3.48 (−3)	3.47 (−3)	3.43 (−3)	3.38 (−3)
20.67	5.47 (−3)	5.70 (−3)	5.79 (−3)	5.82 (−3)	5.82 (−3)	5.79 (−3)
21.00	8.92 (−3)	9.54 (−3)	9.79 (−3)	9.91 (−3)	9.99 (−3)	9.98 (−3)
21.33	1.44 (−2)	1.56 (−2)	1.61 (−2)	1.64 (−2)	1.66 (−2)	1.67 (−2)
21.67	2.32 (−2)	2.52 (−2)	2.62 (−2)	2.68 (−2)	2.74 (−2)	2.76 (−2)
22.00	3.80 (−2)	4.08 (−2)	4.22 (−2)	4.31 (−2)	4.42 (−2)	4.48 (−2)
22.33	6.28 (−2)	6.71 (−2)	6.93 (−2)	7.08 (−2)	7.26 (−2)	7.37 (−2)
22.67	1.05 (−1)	1.11 (−1)	1.15 (−1)	1.17 (−1)	1.19 (−1)	1.20 (−1)
23.00	1.71 (−1)	1.84 (−1)	1.90 (−1)	1.94 (−1)	1.99 (−1)	2.02 (−1)
23.33	2.69 (−1)	3.05 (−1)	3.22 (−1)	3.30 (−1)	3.37 (−1)	3.36 (−1)
23.67	4.11 (−1)	4.89 (−1)	5.27 (−1)	5.48 (−1)	5.68 (−1)	5.73 (−1)
24.00	—	7.68 (−1)	8.43 (−1)	8.90 (−1)	9.43 (−1)	9.68 (−1)
24.33	—	1.20 (+0)	1.34 (+0)	1.43 (+0)	1.54 (+0)	1.61 (+0)
24.67	—	—	2.07 (+0)	2.24 (+0)	2.47 (+0)	2.60 (+0)

The notation '1.27 (−3)' has been used to represent 1.27×10^{-3}.

Table 17. FWHM of Lyman-γ (in nm). $\mu = 0.9$.

log(N_e) (m^{-3})	Temperature (K)					
	5000	10 000	15 000	20 000	30 000	40 000
20.00	2.03 (−3)	2.05 (−3)	2.04 (−3)	2.03 (−3)	1.99 (−3)	1.95 (−3)
20.33	3.33 (−3)	3.46 (−3)	3.49 (−3)	3.49 (−3)	3.45 (−3)	3.39 (−3)
20.67	5.40 (−3)	5.65 (−3)	5.75 (−3)	5.79 (−3)	5.81 (−3)	5.79 (−3)
21.00	8.82 (−3)	9.46 (−3)	9.73 (−3)	9.87 (−3)	9.99 (−3)	1.00 (−2)
21.33	1.42 (−2)	1.54 (−2)	1.59 (−2)	1.62 (−2)	1.64 (−2)	1.65 (−2)
21.67	2.29 (−2)	2.50 (−2)	2.59 (−2)	2.65 (−2)	2.71 (−2)	2.74 (−2)
22.00	3.75 (−2)	4.01 (−2)	4.15 (−2)	4.24 (−2)	4.35 (−2)	4.41 (−2)
22.33	6.23 (−2)	6.64 (−2)	6.86 (−2)	7.00 (−2)	7.18 (−2)	7.29 (−2)
22.67	1.04 (−1)	1.10 (−1)	1.14 (−1)	1.16 (−1)	1.18 (−1)	1.19 (−1)
23.00	1.71 (−1)	1.83 (−1)	1.89 (−1)	1.92 (−1)	1.97 (−1)	1.99 (−1)
23.33	2.68 (−1)	3.04 (−1)	3.20 (−1)	3.28 (−1)	3.34 (−1)	3.33 (−1)
23.67	4.10 (−1)	4.88 (−1)	5.26 (−1)	5.47 (−1)	5.65 (−1)	5.69 (−1)
24.00	—	7.67 (−1)	8.42 (−1)	8.88 (−1)	9.40 (−1)	9.64 (−1)
24.33	—	1.20 (+0)	1.34 (+0)	1.42 (+0)	1.52 (+0)	1.57 (+0)
24.67	—	—	2.06 (+0)	2.24 (+0)	2.46 (+0)	2.59 (+0)

The notation '1.27 (−3)' has been used to represent 1.27×10^{-3}.

4. Results

The simulations in this work have been carried out for electron densities between 10^{20} and 4.64×10^{24} m^{-3} with a one-third of a decade regular spacing. As for the reduced mass, the following values have been included in the calculations: $\mu = 0.5$ (which represents a pure hydrogen plasma), 0.8 (helium perturbers), 0.9, 1.0 (which gather all the possible values of μ for a hydrogen emitter and any perturbing ion or a pure deuterium plasma), and $\mu = 2.0$, which applies for a deuterium emitter surrounded by heavy perturbing ions. Calculations have also been carried out for some intermediate μ values—0.6, 1.25, 1.5 and

Table 18. FWHM of Lyman-γ (in nm). $\mu = 1$.

log(N_e)	Temperature (K)					
(m^{-3})	5000	10 000	15 000	20 000	30 000	40 000
20.00	2.02 (−3)	2.06 (−3)	2.06 (−3)	2.05 (−3)	2.02 (−3)	1.98 (−3)
20.33	3.27 (−3)	3.45 (−3)	3.50 (−3)	3.51 (−3)	3.47 (−3)	3.42 (−3)
20.67	5.33 (−3)	5.61 (−3)	5.72 (−3)	5.78 (−3)	5.82 (−3)	5.82 (−3)
21.00	8.72 (−3)	9.38 (−3)	9.65 (−3)	9.79 (−3)	9.91 (−3)	9.93 (−3)
21.33	1.40 (−2)	1.52 (−2)	1.57 (−2)	1.60 (−2)	1.63 (−2)	1.64 (−2)
21.67	2.26 (−2)	2.46 (−2)	2.55 (−2)	2.61 (−2)	2.67 (−2)	2.70 (−2)
22.00	3.71 (−2)	3.97 (−2)	4.10 (−2)	4.19 (−2)	4.30 (−2)	4.37 (−2)
22.33	6.18 (−2)	6.60 (−2)	6.82 (−2)	6.96 (−2)	7.15 (−2)	7.27 (−2)
22.67	1.04 (−1)	1.10 (−1)	1.13 (−1)	1.14 (−1)	1.16 (−1)	1.17 (−1)
23.00	1.70 (−1)	1.82 (−1)	1.88 (−1)	1.91 (−1)	1.94 (−1)	1.95 (−1)
23.33	2.68 (−1)	3.04 (−1)	3.19 (−1)	3.27 (−1)	3.32 (−1)	3.31 (−1)
23.67	4.09 (−1)	4.87 (−1)	5.25 (−1)	5.45 (−1)	5.63 (−1)	5.66 (−1)
24.00	—	7.66 (−1)	8.40 (−1)	8.86 (−1)	9.38 (−1)	9.62 (−1)
24.33	—	1.19 (+0)	1.33 (+0)	1.42 (+0)	1.52 (+0)	1.56 (+0)
24.67	—	—	2.06 (+0)	2.23 (+0)	2.45 (+0)	2.58 (+0)

The notation '1.27 (−3)' has been used to represent 1.27×10^{-3}.

Table 19. FWHM of Lyman-γ (in nm). $\mu = 2$.

log(N_e)	Temperature (K)					
(m^{-3})	5000	10 000	15 000	20 000	30 000	40 000
20.00	1.90 (−3)	2.05 (−3)	2.09 (−3)	2.10 (−3)	2.08 (−3)	2.04 (−3)
20.33	3.03 (−3)	3.33 (−3)	3.45 (−3)	3.50 (−3)	3.53 (−3)	3.52 (−3)
20.67	4.85 (−3)	5.30 (−3)	5.51 (−3)	5.63 (−3)	5.75 (−3)	5.81 (−3)
21.00	7.91 (−3)	8.57 (−3)	8.89 (−3)	9.10 (−3)	9.34 (−3)	9.49 (−3)
21.33	1.27 (−2)	1.37 (−2)	1.42 (−2)	1.46 (−2)	1.51 (−2)	1.54 (−2)
21.67	2.07 (−2)	2.25 (−2)	2.34 (−2)	2.40 (−2)	2.48 (−2)	2.54 (−2)
22.00	3.47 (−2)	3.62 (−2)	3.72 (−2)	3.79 (−2)	3.91 (−2)	4.00 (−2)
22.33	5.98 (−2)	6.13 (−2)	6.23 (−2)	6.31 (−2)	6.44 (−2)	6.55 (−2)
22.67	1.02 (−1)	1.05 (−1)	1.06 (−1)	1.07 (−1)	1.07 (−1)	1.07 (−1)
23.00	1.62 (−1)	1.77 (−1)	1.83 (−1)	1.85 (−1)	1.84 (−1)	1.80 (−1)
23.33	2.64 (−1)	2.94 (−1)	3.07 (−1)	3.13 (−1)	3.16 (−1)	3.13 (−1)
23.67	4.08 (−1)	4.80 (−1)	5.14 (−1)	5.32 (−1)	5.46 (−1)	5.47 (−1)
24.00	—	7.61 (−1)	8.28 (−1)	8.70 (−1)	9.17 (−1)	9.41 (−1)
24.33	—	1.19 (+0)	1.32 (+0)	1.40 (+0)	1.49 (+0)	1.53 (+0)
24.67	—	—	2.03 (+0)	2.21 (+0)	2.43 (+0)	2.55 (+0)

The notation '1.27 (−3)' has been used to represent 1.27×10^{-3}.

1.75—in order to study the functional dependence of the relevant parameters on the reduced mass. As for the ρ parameter, which enables the determination of the temperature from the electronic density, values have been taken in the range 0.1–1.0, at regular jumps of 0.1. Not every possible density case has been calculated for every ρ since the temperature corresponding to a high-density value might be unreasonably high while the one for a low-density case could be ridiculous. Table 1 summarizes all the considered cases and shows the temperatures for every simulated N_e and ρ condition.

Two calculation series were carried out. The results of the first one were primarily used to provide information about the optimum values of some simulation parameters, specially

Table 20. FWHM of Balmer-α (in nm). $\mu = 0.5$.

log(N_e) (m^{-3})	Temperature (K)					
	5000	10 000	15 000	20 000	30 000	40 000
20.00	1.40 (−2)	1.30 (−2)	1.21 (−2)	1.13 (−2)	9.82 (−3)	8.53 (−3)
20.33	2.41 (−2)	2.34 (−2)	2.23 (−2)	2.13 (−2)	1.93 (−2)	1.75 (−2)
20.67	3.95 (−2)	4.08 (−2)	4.03 (−2)	3.93 (−2)	3.69 (−2)	3.44 (−2)
21.00	6.36 (−2)	6.71 (−2)	6.78 (−2)	6.75 (−2)	6.58 (−2)	6.36 (−2)
21.33	1.01 (−1)	1.09 (−1)	1.12 (−1)	1.13 (−1)	1.13 (−1)	1.12 (−1)
21.67	1.58 (−1)	1.75 (−1)	1.82 (−1)	1.86 (−1)	1.89 (−1)	1.89 (−1)
22.00	2.47 (−1)	2.76 (−1)	2.90 (−1)	2.99 (−1)	3.08 (−1)	3.13 (−1)
22.33	3.89 (−1)	4.35 (−1)	4.60 (−1)	4.76 (−1)	4.95 (−1)	5.06 (−1)
22.67	6.20 (−1)	6.86 (−1)	7.24 (−1)	7.51 (−1)	7.88 (−1)	8.14 (−1)
23.00	1.02 (+0)	1.10 (+0)	1.15 (+0)	1.19 (+0)	1.25 (+0)	1.29 (+0)
23.33	1.68 (+0)	1.79 (+0)	1.86 (+0)	1.91 (+0)	1.99 (+0)	2.05 (+0)
23.67	2.83 (+0)	2.97 (+0)	3.05 (+0)	3.12 (+0)	3.21 (+0)	3.29 (+0)
24.00	—	5.00 (+0)	5.12 (+0)	5.20 (+0)	5.30 (+0)	5.37 (+0)
24.33	—	8.53 (+0)	8.69 (+0)	8.79 (+0)	8.89 (+0)	8.94 (+0)
24.67	—	—	1.47 (+1)	1.50 (+1)	1.52 (+1)	1.53 (+1)

The notation '1.27 (−3)' has been used to represent 1.27×10^{-3}.

Table 21. FWHM of Balmer-α (in nm). $\mu = 0.8$.

log(N_e) (m^{-3})	Temperature (K)					
	5000	10 000	15 000	20 000	30 000	40 000
20.00	1.44 (−2)	1.40 (−2)	1.33 (−2)	1.26 (−2)	1.12 (−2)	9.88 (−3)
20.33	2.38 (−2)	2.44 (−2)	2.39 (−2)	2.32 (−2)	2.15 (−2)	1.98 (−2)
20.67	3.82 (−2)	4.07 (−2)	4.10 (−2)	4.07 (−2)	3.93 (−2)	3.76 (−2)
21.00	6.01 (−2)	6.49 (−2)	6.66 (−2)	6.72 (−2)	6.72 (−2)	6.64 (−2)
21.33	9.41 (−2)	1.04 (−1)	1.08 (−1)	1.10 (−1)	1.12 (−1)	1.13 (−1)
21.67	1.46 (−1)	1.63 (−1)	1.71 (−1)	1.76 (−1)	1.82 (−1)	1.85 (−1)
22.00	2.29 (−1)	2.55 (−1)	2.70 (−1)	2.79 (−1)	2.90 (−1)	2.98 (−1)
22.33	3.61 (−1)	4.01 (−1)	4.24 (−1)	4.39 (−1)	4.60 (−1)	4.74 (−1)
22.67	5.83 (−1)	6.35 (−1)	6.68 (−1)	6.93 (−1)	7.30 (−1)	7.58 (−1)
23.00	9.77 (−1)	1.02 (+0)	1.06 (+0)	1.09 (+0)	1.15 (+0)	1.21 (+0)
23.33	1.63 (+0)	1.70 (+0)	1.74 (+0)	1.78 (+0)	1.84 (+0)	1.88 (+0)
23.67	2.78 (+0)	2.86 (+0)	2.92 (+0)	2.96 (+0)	3.02 (+0)	3.06 (+0)
24.00	—	4.88 (+0)	4.96 (+0)	5.01 (+0)	5.06 (+0)	5.09 (+0)
24.33	—	8.34 (+0)	8.50 (+0)	8.57 (+0)	8.59 (+0)	8.54 (+0)
24.67	—	—	1.45 (+1)	1.46 (+1)	1.48 (+1)	1.48 (+1)

The notation '1.27 (−3)' has been used to represent 1.27×10^{-3}.

the duration of all the line profile calculations in terms of simulation time steps. The second series included three or four independent blocks of 5000 simulation runs each, in order to estimate the dispersion of the results. Table 2 details all the conditions of the processed cases. The final tabulated data were obtained from the Fourier transform of the autocorrelation functions which accumulated the ones obtained in the whole set of runs. The individual blocks of 5000 runs were only taken into account when the error bars were to be estimated.

In order to have control over the influence of the number of particles used in the simulations, a set of calculations using 100, 500 and 2700 particles were carried out in the

Table 22. FWHM of Balmer-α (in nm). $\mu = 0.9$.

log(N_e) (m^{-3})	Temperature (K)					
	5000	10 000	15 000	20 000	30 000	40 000
20.00	1.45 (−2)	1.42 (−2)	1.35 (−2)	1.29 (−2)	1.15 (−2)	1.03 (−2)
20.33	2.36 (−2)	2.44 (−2)	2.40 (−2)	2.34 (−2)	2.20 (−2)	2.04 (−2)
20.67	3.76 (−2)	4.04 (−2)	4.10 (−2)	4.08 (−2)	3.97 (−2)	3.82 (−2)
21.00	5.90 (−2)	6.40 (−2)	6.59 (−2)	6.67 (−2)	6.71 (−2)	6.67 (−2)
21.33	9.22 (−2)	1.02 (−1)	1.06 (−1)	1.09 (−1)	1.11 (−1)	1.12 (−1)
21.67	1.43 (−1)	1.60 (−1)	1.69 (−1)	1.74 (−1)	1.80 (−1)	1.84 (−1)
22.00	2.24 (−1)	2.50 (−1)	2.64 (−1)	2.73 (−1)	2.85 (−1)	2.93 (−1)
22.33	3.55 (−1)	3.93 (−1)	4.15 (−1)	4.30 (−1)	4.51 (−1)	4.65 (−1)
22.67	5.76 (−1)	6.21 (−1)	6.52 (−1)	6.75 (−1)	7.13 (−1)	7.42 (−1)
23.00	9.65 (−1)	1.01 (+0)	1.04 (+0)	1.08 (+0)	1.13 (+0)	1.18 (+0)
23.33	1.62 (+0)	1.68 (+0)	1.72 (+0)	1.76 (+0)	1.81 (+0)	1.86 (+0)
23.67	2.76 (+0)	2.84 (+0)	2.89 (+0)	2.92 (+0)	2.97 (+0)	3.01 (+0)
24.00	—	4.86 (+0)	4.92 (+0)	4.96 (+0)	5.00 (+0)	5.01 (+0)
24.33	—	8.31 (+0)	8.45 (+0)	8.50 (+0)	8.49 (+0)	8.41 (+0)
24.67	—	—	1.44 (+1)	1.46 (+1)	1.47 (+1)	1.47 (+1)

The notation '1.27 (−3)' has been used to represent 1.27×10^{-3}.

Table 23. FWHM of Balmer-α (in nm). $\mu = 1$.

log(N_e) (m^{-3})	Temperature (K)					
	5000	10 000	15 000	20 000	30 000	40 000
20.00	1.44 (−2)	1.43 (−2)	1.37 (−2)	1.31 (−2)	1.18 (−2)	1.06 (−2)
20.33	2.34 (−2)	2.44 (−2)	2.42 (−2)	2.37 (−2)	2.24 (−2)	2.10 (−2)
20.67	3.70 (−2)	4.01 (−2)	4.08 (−2)	4.08 (−2)	3.99 (−2)	3.86 (−2)
21.00	5.82 (−2)	6.34 (−2)	6.54 (−2)	6.64 (−2)	6.71 (−2)	6.70 (−2)
21.33	9.06 (−2)	1.00 (−1)	1.05 (−1)	1.08 (−1)	1.11 (−1)	1.12 (−1)
21.67	1.41 (−1)	1.58 (−1)	1.66 (−1)	1.72 (−1)	1.78 (−1)	1.82 (−1)
22.00	2.20 (−1)	2.46 (−1)	2.60 (−1)	2.69 (−1)	2.82 (−1)	2.90 (−1)
22.33	3.50 (−1)	3.86 (−1)	4.08 (−1)	4.22 (−1)	4.43 (−1)	4.58 (−1)
22.67	5.70 (−1)	6.11 (−1)	6.40 (−1)	6.63 (−1)	6.99 (−1)	7.28 (−1)
23.00	9.58 (−1)	9.92 (−1)	1.02 (+0)	1.05 (+0)	1.11 (+0)	1.15 (+0)
23.33	1.61 (+0)	1.66 (+0)	1.70 (+0)	1.73 (+0)	1.78 (+0)	1.83 (+0)
23.67	2.77 (+0)	2.82 (+0)	2.86 (+0)	2.89 (+0)	2.93 (+0)	2.96 (+0)
24.00	—	4.83 (+0)	4.88 (+0)	4.91 (+0)	4.94 (+0)	4.95 (+0)
24.33	—	8.27 (+0)	8.39 (+0)	8.44 (+0)	8.42 (+0)	8.35 (+0)
24.67	—	—	1.44 (+1)	1.46 (+1)	1.46 (+1)	1.46 (+1)

The notation '1.27 (−3)' has been used to represent 1.27×10^{-3}.

most critical $\rho = 0.2$ value of the ones included in series 1. Results for the Lyman alpha line, where the possible differences would be most clearly seen, show width fluctuations between 0.4% and 2% for $N_e = 10^{21}$ m^{-3} and between 1.5% and 3% for $N_e = 4.6 \times 10^{22}$ m^{-3}. These discrepancies are of the same order to that found between two complete blocks of 5000 runs in the same plasma conditions, which clearly excuses the necessity of including more particles in these kind of simulations. Anyway, it is always observed that width results slightly decrease as the number of particles inside the simulation sphere grows. This sustains the assertion that the width results presented in the tables of this work will be above the ones obtained in an 'ideal' simulation by as much as 3%. For a more detailed analysis

Table 24. FWHM of Balmer-α (in nm). $\mu = 2$.

log(N_e) (m^{-3})	Temperature (K)					
	5000	10 000	15 000	20 000	30 000	40 000
20.00	1.38 (−2)	1.43 (−2)	1.43 (−2)	1.41 (−2)	1.35 (−2)	1.29 (−2)
20.33	2.20 (−2)	2.34 (−2)	2.38 (−2)	2.39 (−2)	2.37 (−2)	2.33 (−2)
20.67	3.34 (−2)	3.74 (−2)	3.90 (−2)	3.98 (−2)	4.02 (−2)	4.01 (−2)
21.00	5.15 (−2)	5.71 (−2)	6.01 (−2)	6.21 (−2)	6.48 (−2)	6.65 (−2)
21.33	7.96 (−2)	8.87 (−2)	9.39 (−2)	9.75 (−2)	1.03 (−1)	1.06 (−1)
21.67	1.23 (−1)	1.38 (−1)	1.46 (−1)	1.53 (−1)	1.61 (−1)	1.68 (−1)
22.00	1.96 (−1)	2.15 (−1)	2.27 (−1)	2.36 (−1)	2.49 (−1)	2.60 (−1)
22.33	3.17 (−1)	3.41 (−1)	3.57 (−1)	3.70 (−1)	3.89 (−1)	4.04 (−1)
22.67	5.30 (−1)	5.51 (−1)	5.69 (−1)	5.86 (−1)	6.14 (−1)	6.39 (−1)
23.00	9.10 (−1)	9.14 (−1)	9.28 (−1)	9.44 (−1)	9.79 (−1)	1.01 (+0)
23.33	1.56 (+0)	1.56 (+0)	1.57 (+0)	1.58 (+0)	1.60 (+0)	1.62 (+0)
23.67	2.71 (+0)	2.71 (+0)	2.70 (+0)	2.70 (+0)	2.70 (+0)	2.70 (+0)
24.00	—	4.72 (+0)	4.71 (+0)	4.69 (+0)	4.65 (+0)	4.61 (+0)
24.33	—	8.18 (+0)	8.21 (+0)	8.19 (+0)	8.11 (+0)	7.99 (+0)
24.67	—	—	1.42 (+1)	1.43 (+1)	1.43 (+1)	1.41 (+1)

The notation '1.27 (−3)' has been used to represent 1.27×10^{-3}.

Table 25. FWHM of Balmer-β (in nm). $\mu = 0.5$.

log(N_e) (m^{-3})	Temperature (K)					
	5000	10 000	15 000	20 000	30 000	40 000
20.00	4.23 (−2)	3.97 (−2)	3.78 (−2)	3.63 (−2)	3.38 (−2)	3.18 (−2)
20.33	7.47 (−2)	7.05 (−2)	6.76 (−2)	6.54 (−2)	6.19 (−2)	5.91 (−2)
20.67	1.25 (−1)	1.24 (−1)	1.22 (−1)	1.19 (−1)	1.14 (−1)	1.09 (−1)
21.00	2.12 (−1)	2.16 (−1)	2.15 (−1)	2.12 (−1)	2.05 (−1)	1.98 (−1)
21.33	3.52 (−1)	3.64 (−1)	3.66 (−1)	3.64 (−1)	3.59 (−1)	3.52 (−1)
21.67	5.85 (−1)	6.10 (−1)	6.18 (−1)	6.20 (−1)	6.17 (−1)	6.11 (−1)
22.00	9.68 (−1)	1.02 (+0)	1.04 (+0)	1.05 (+0)	1.05 (+0)	1.05 (+0)
22.33	1.61 (+0)	1.69 (+0)	1.73 (+0)	1.75 (+0)	1.77 (+0)	1.77 (+0)
22.67	2.66 (+0)	2.83 (+0)	2.90 (+0)	2.94 (+0)	2.97 (+0)	2.98 (+0)
23.00	4.30 (+0)	4.73 (+0)	4.90 (+0)	4.97 (+0)	4.98 (+0)	4.92 (+0)
23.33	6.95 (+0)	7.81 (+0)	8.18 (+0)	8.37 (+0)	8.49 (+0)	8.45 (+0)
23.67	1.11 (+1)	1.28 (+1)	1.36 (+1)	1.40 (+1)	1.44 (+1)	1.45 (+1)
24.00	—	2.05 (+1)	2.23 (+1)	2.33 (+1)	2.40 (+1)	2.41 (+1)
24.33	—	3.25 (+1)	3.61 (+1)	3.81 (+1)	3.99 (+1)	4.01 (+1)
24.67	—	—	5.77 (+1)	6.14 (+1)	6.56 (+1)	6.75 (+1)

The notation '1.27 (−3)' has been used to represent 1.27×10^{-3}.

of the influence of N_p on the simulations, we refer the reader to [17].

The use of the so called *reduced width* is a common practice in order to quantify the widths of spectral lines. This is given by the expression

$$\Delta\alpha = \frac{\Delta\lambda}{F_0}$$
$$= 8.106 \times 10^{13} N_e^{2/3}\Delta\lambda \qquad (N_e \text{ in m}^{-3}, \Delta\lambda \text{ in nm}).$$

where F_0 is the Holtsmark normal field. This representation aims to eliminate from the lines the width of the strongest functional dependence on the electron density, which is related

Table 26. FWHM of Balmer-β (in nm). $\mu = 0.8$.

log(N_e) (m^{-3})	Temperature (K)					
	5000	10 000	15 000	20 000	30 000	40 000
20.00	4.41 (−2)	4.19 (−2)	4.03 (−2)	3.89 (−2)	3.68 (−2)	3.50 (−2)
20.33	7.62 (−2)	7.34 (−2)	7.13 (−2)	6.94 (−2)	6.64 (−2)	6.37 (−2)
20.67	1.26 (−1)	1.28 (−1)	1.27 (−1)	1.25 (−1)	1.21 (−1)	1.16 (−1)
21.00	2.11 (−1)	2.18 (−1)	2.18 (−1)	2.17 (−1)	2.13 (−1)	2.07 (−1)
21.33	3.49 (−1)	3.62 (−1)	3.66 (−1)	3.66 (−1)	3.64 (−1)	3.59 (−1)
21.67	5.79 (−1)	6.03 (−1)	6.12 (−1)	6.15 (−1)	6.16 (−1)	6.12 (−1)
22.00	9.59 (−1)	1.00 (+0)	1.02 (+0)	1.03 (+0)	1.04 (+0)	1.04 (+0)
22.33	1.59 (+0)	1.67 (+0)	1.71 (+0)	1.73 (+0)	1.75 (+0)	1.76 (+0)
22.67	2.64 (+0)	2.80 (+0)	2.87 (+0)	2.91 (+0)	2.94 (+0)	2.95 (+0)
23.00	4.28 (+0)	4.70 (+0)	4.87 (+0)	4.93 (+0)	4.94 (+0)	4.87 (+0)
23.33	6.94 (+0)	7.77 (+0)	8.13 (+0)	8.30 (+0)	8.39 (+0)	8.34 (+0)
23.67	1.11 (+1)	1.27 (+1)	1.35 (+1)	1.39 (+1)	1.43 (+1)	1.44 (+1)
24.00	—	2.05 (+1)	2.22 (+1)	2.31 (+1)	2.39 (+1)	2.40 (+1)
24.33	—	3.25 (+1)	3.60 (+1)	3.80 (+1)	3.97 (+1)	3.99 (+1)
24.67	—	—	5.75 (+1)	6.13 (+1)	6.55 (+1)	6.74 (+1)

The notation '1.27 (−3)' has been used to represent 1.27×10^{-3}.

Table 27. FWHM of Balmer-β (in nm). $\mu = 0.9$.

log(N_e) (m^{-3})	Temperature (K)					
	5000	10 000	15 000	20 000	30 000	40 000
20.00	4.44 (−2)	4.24 (−2)	4.09 (−2)	3.96 (−2)	3.75 (−2)	3.57 (−2)
20.33	7.64 (−2)	7.41 (−2)	7.22 (−2)	7.04 (−2)	6.74 (−2)	6.48 (−2)
20.67	1.26 (−1)	1.29 (−1)	1.28 (−1)	1.26 (−1)	1.22 (−1)	1.18 (−1)
21.00	2.11 (−1)	2.17 (−1)	2.18 (−1)	2.17 (−1)	2.14 (−1)	2.09 (−1)
21.33	3.48 (−1)	3.61 (−1)	3.66 (−1)	3.66 (−1)	3.64 (−1)	3.60 (−1)
21.67	5.76 (−1)	6.01 (−1)	6.10 (−1)	6.14 (−1)	6.15 (−1)	6.12 (−1)
22.00	9.56 (−1)	9.99 (−1)	1.02 (+0)	1.03 (+0)	1.04 (+0)	1.04 (+0)
22.33	1.59 (+0)	1.67 (+0)	1.70 (+0)	1.72 (+0)	1.75 (+0)	1.75 (+0)
22.67	2.64 (+0)	2.80 (+0)	2.87 (+0)	2.90 (+0)	2.94 (+0)	2.94 (+0)
23.00	4.28 (+0)	4.70 (+0)	4.86 (+0)	4.92 (+0)	4.93 (+0)	4.86 (+0)
23.33	6.95 (+0)	7.77 (+0)	8.12 (+0)	8.29 (+0)	8.38 (+0)	8.32 (+0)
23.67	1.11 (+1)	1.27 (+1)	1.35 (+1)	1.39 (+1)	1.43 (+1)	1.44 (+1)
24.00	—	2.05 (+1)	2.22 (+1)	2.31 (+1)	2.39 (+1)	2.39 (+1)
24.33	—	3.25 (+1)	3.60 (+1)	3.79 (+1)	3.96 (+1)	3.99 (+1)
24.67	—	—	5.74 (+1)	6.13 (+1)	6.56 (+1)	6.74 (+1)

The notation '1.27 (−3)' has been used to represent 1.27×10^{-3}.

to the statistics of the quasistatic ion field. It is already well known that when the effects of the correlation between the charged particles in the plasma are taken into account—as is the case in Hooper's distribution [29]—the typical field values seen by the emitter are smaller as the Debye radius decreases while the electron density remains constant. That is to say, the quasistatic fields decrease when ρ grows. As we shall see, it is also convenient to remove this smooth dependence of the width with the temperature. To this end, a new reduced width $\Delta\Omega$ shall be defined with the expression

$$\frac{\Delta\lambda_{1/2}}{\lambda_0} = \frac{\Delta\omega_{1/2}}{\omega_0} = \frac{1}{\omega_0}\frac{3}{2\hbar}nqa_0 E_0 \times \Delta\Omega, \qquad (40)$$

Table 28. FWHM of Balmer-β (in nm). $\mu = 1$.

log(N_e) (m^{-3})	Temperature (K)					
	5000	10 000	15 000	20 000	30 000	40 000
20.00	4.46 (−2)	4.27 (−2)	4.13 (−2)	4.00 (−2)	3.80 (−2)	3.63 (−2)
20.33	7.65 (−2)	7.48 (−2)	7.31 (−2)	7.14 (−2)	6.84 (−2)	6.58 (−2)
20.67	1.26 (−1)	1.29 (−1)	1.29 (−1)	1.27 (−1)	1.23 (−1)	1.19 (−1)
21.00	2.10 (−1)	2.17 (−1)	2.18 (−1)	2.17 (−1)	2.14 (−1)	2.10 (−1)
21.33	3.47 (−1)	3.60 (−1)	3.64 (−1)	3.66 (−1)	3.64 (−1)	3.61 (−1)
21.67	5.75 (−1)	5.99 (−1)	6.09 (−1)	6.13 (−1)	6.15 (−1)	6.12 (−1)
22.00	9.52 (−1)	9.97 (−1)	1.02 (+0)	1.03 (+0)	1.04 (+0)	1.04 (+0)
22.33	1.59 (+0)	1.66 (+0)	1.70 (+0)	1.72 (+0)	1.74 (+0)	1.75 (+0)
22.67	2.64 (+0)	2.79 (+0)	2.86 (+0)	2.90 (+0)	2.93 (+0)	2.94 (+0)
23.00	4.28 (+0)	4.69 (+0)	4.85 (+0)	4.91 (+0)	4.91 (+0)	4.84 (+0)
23.33	6.94 (+0)	7.76 (+0)	8.11 (+0)	8.28 (+0)	8.36 (+0)	8.30 (+0)
23.67	1.11 (+1)	1.27 (+1)	1.35 (+1)	1.39 (+1)	1.43 (+1)	1.43 (+1)
24.00	—	2.05 (+1)	2.22 (+1)	2.31 (+1)	2.39 (+1)	2.39 (+1)
24.33	—	3.25 (+1)	3.60 (+1)	3.79 (+1)	3.96 (+1)	3.99 (+1)
24.67	—	—	5.75 (+1)	6.13 (+1)	6.55 (+1)	6.74 (+1)

The notation '1.27 (−3)' has been used to represent 1.27×10^{-3}.

Table 29. FWHM of Balmer-β (in nm). $\mu = 2$.

log(N_e) (m^{-3})	Temperature (K)					
	5000	10 000	15 000	20 000	30 000	40 000
20.00	4.55 (−2)	4.50 (−2)	4.42 (−2)	4.34 (−2)	4.17 (−2)	4.01 (−2)
20.33	7.62 (−2)	7.64 (−2)	7.58 (−2)	7.51 (−2)	7.34 (−2)	7.19 (−2)
20.67	1.23 (−1)	1.28 (−1)	1.29 (−1)	1.29 (−1)	1.28 (−1)	1.26 (−1)
21.00	2.05 (−1)	2.13 (−1)	2.16 (−1)	2.17 (−1)	2.16 (−1)	2.15 (−1)
21.33	3.39 (−1)	3.53 (−1)	3.59 (−1)	3.62 (−1)	3.64 (−1)	3.64 (−1)
21.67	5.64 (−1)	5.88 (−1)	5.99 (−1)	6.04 (−1)	6.09 (−1)	6.11 (−1)
22.00	9.41 (−1)	9.79 (−1)	9.97 (−1)	1.01 (+0)	1.02 (+0)	1.02 (+0)
22.33	1.58 (+0)	1.64 (+0)	1.67 (+0)	1.69 (+0)	1.71 (+0)	1.72 (+0)
22.67	2.62 (+0)	2.76 (+0)	2.82 (+0)	2.85 (+0)	2.87 (+0)	2.88 (+0)
23.00	4.27 (+0)	4.67 (+0)	4.81 (+0)	4.86 (+0)	4.85 (+0)	4.76 (+0)
23.33	6.89 (+0)	7.73 (+0)	8.08 (+0)	8.24 (+0)	8.32 (+0)	8.25 (+0)
23.67	1.10 (+1)	1.27 (+1)	1.35 (+1)	1.39 (+1)	1.42 (+1)	1.42 (+1)
24.00	—	2.05 (+1)	2.21 (+1)	2.30 (+1)	2.38 (+1)	2.38 (+1)
24.33	—	3.24 (+1)	3.59 (+1)	3.79 (+1)	3.96 (+1)	3.98 (+1)
24.67	—	—	5.74 (+1)	6.12 (+1)	6.55 (+1)	6.73 (+1)

The notation '1.27 (−3)' has been used to represent 1.27×10^{-3}.

so that $\Delta\Omega$ is a normalized quantity that adimensionally accounts for the width. The magnitudes n, q and a_0 stand for the principal quantum number of the upper level of the transition, the charge of the electron and the Bohr radius, respectively. The electric field E_0 is a typical field which, as can be shown, evaluates to

$$E_0 = \frac{1.6}{1 + 1.25\rho} \frac{q}{4\pi\epsilon_0} \left(\frac{4\pi N_e}{3}\right)^{\frac{2}{3}};$$ (41)

which includes a smooth temperature dependence through the parameter ρ. The results obtained in the simulations have been processed following this criterion, using $\Delta\Omega$. This

Table 30. FWHM of Balmer-γ (in nm). $\mu = 0.5$.

log(N_e) (m^{-3})	Temperature (K)					
	5000	10 000	15 000	20 000	30 000	40 000
20.00	5.87 (−2)	5.91 (−2)	5.88 (−2)	5.82 (−2)	5.69 (−2)	5.55 (−2)
20.33	9.78 (−2)	9.96 (−2)	9.97 (−2)	9.94 (−2)	9.81 (−2)	9.66 (−2)
20.67	1.61 (−1)	1.67 (−1)	1.68 (−1)	1.69 (−1)	1.69 (−1)	1.68 (−1)
21.00	2.72 (−1)	2.84 (−1)	2.88 (−1)	2.90 (−1)	2.89 (−1)	2.86 (−1)
21.33	4.48 (−1)	4.71 (−1)	4.79 (−1)	4.83 (−1)	4.85 (−1)	4.83 (−1)
21.67	7.44 (−1)	7.84 (−1)	8.01 (−1)	8.10 (−1)	8.16 (−1)	8.16 (−1)
22.00	1.22 (+0)	1.30 (+0)	1.34 (+0)	1.36 (+0)	1.37 (+0)	1.38 (+0)
22.33	2.02 (+0)	2.16 (+0)	2.22 (+0)	2.26 (+0)	2.30 (+0)	2.32 (+0)
22.67	3.30 (+0)	3.59 (+0)	3.73 (+0)	3.80 (+0)	3.86 (+0)	3.88 (+0)
23.00	5.20 (+0)	5.89 (+0)	6.20 (+0)	6.37 (+0)	6.51 (+0)	6.54 (+0)
23.33	8.16 (+0)	9.56 (+0)	1.02 (+1)	1.06 (+1)	1.09 (+1)	1.10 (+1)
23.67	1.26 (+1)	1.52 (+1)	1.65 (+1)	1.73 (+1)	1.82 (+1)	1.85 (+1)
24.00	—	2.37 (+1)	2.64 (+1)	2.80 (+1)	2.97 (+1)	3.04 (+1)
24.33	—	3.59 (+1)	4.12 (+1)	4.44 (+1)	4.79 (+1)	4.95 (+1)
24.67	—	—	6.24 (+1)	6.86 (+1)	7.61 (+1)	8.03 (+1)

The notation '1.27 (−3)' has been used to represent 1.27×10^{-3}.

Table 31. FWHM of Balmer-γ (in nm). $\mu = 0.8$.

log(N_e) (m^{-3})	Temperature (K)					
	5000	10 000	15 000	20 000	30 000	40 000
20.00	5.76 (−2)	5.91 (−2)	5.93 (−2)	5.91 (−2)	5.83 (−2)	5.73 (−2)
20.33	9.48 (−2)	9.88 (−2)	1.00 (−1)	1.00 (−1)	10.00 (−2)	9.91 (−2)
20.67	1.58 (−1)	1.63 (−1)	1.65 (−1)	1.66 (−1)	1.67 (−1)	1.67 (−1)
21.00	2.64 (−1)	2.76 (−1)	2.80 (−1)	2.82 (−1)	2.83 (−1)	2.82 (−1)
21.33	4.37 (−1)	4.56 (−1)	4.64 (−1)	4.68 (−1)	4.72 (−1)	4.72 (−1)
21.67	7.27 (−1)	7.59 (−1)	7.73 (−1)	7.82 (−1)	7.90 (−1)	7.93 (−1)
22.00	1.20 (+0)	1.27 (+0)	1.30 (+0)	1.32 (+0)	1.33 (+0)	1.34 (+0)
22.33	2.00 (+0)	2.12 (+0)	2.18 (+0)	2.22 (+0)	2.25 (+0)	2.27 (+0)
22.67	3.28 (+0)	3.54 (+0)	3.66 (+0)	3.73 (+0)	3.78 (+0)	3.78 (+0)
23.00	5.19 (+0)	5.83 (+0)	6.12 (+0)	6.28 (+0)	6.40 (+0)	6.41 (+0)
23.33	8.13 (+0)	9.51 (+0)	1.02 (+1)	1.05 (+1)	1.08 (+1)	1.09 (+1)
23.67	1.25 (+1)	1.51 (+1)	1.65 (+1)	1.72 (+1)	1.80 (+1)	1.83 (+1)
24.00	—	2.36 (+1)	2.63 (+1)	2.79 (+1)	2.95 (+1)	3.02 (+1)
24.33	—	3.56 (+1)	4.09 (+1)	4.42 (+1)	4.77 (+1)	4.93 (+1)
24.67	—	—	6.22 (+1)	6.82 (+1)	7.56 (+1)	7.99 (+1)

The notation '1.27 (−3)' has been used to represent 1.27×10^{-3}.

has been a very convenient decision for the temperature interpolation in terms of ρ for every electron density. Once the value of $\Delta\Omega$ has been extracted from the simulation results, a fitting function of type

$$\rho\Delta\Omega = P_2(\rho), \qquad (42)$$

is used, where $P_2(x)$ is a polynomial of degree 2. This fit is done for a fixed value of the electron density. Figure 1 shows a typical example. The values appearing in tables 5–34 have then been obtained from the ρ interpolation for the selected temperatures according to these fits. From our point of view, this parametrization should always be used when

Table 32. FWHM of Balmer-γ (in nm). $\mu = 0.9$.

log(N_e) (m^{-3})	Temperature (K)					
	5000	10 000	15 000	20 000	30 000	40 000
20.00	5.72 (−2)	5.93 (−2)	5.98 (−2)	5.96 (−2)	5.88 (−2)	5.78 (−2)
20.33	9.42 (−2)	9.83 (−2)	9.96 (−2)	1.00 (−1)	9.97 (−2)	9.89 (−2)
20.67	1.56 (−1)	1.62 (−1)	1.64 (−1)	1.65 (−1)	1.66 (−1)	1.66 (−1)
21.00	2.62 (−1)	2.73 (−1)	2.78 (−1)	2.80 (−1)	2.81 (−1)	2.81 (−1)
21.33	4.34 (−1)	4.54 (−1)	4.62 (−1)	4.67 (−1)	4.71 (−1)	4.72 (−1)
21.67	7.23 (−1)	7.53 (−1)	7.67 (−1)	7.75 (−1)	7.83 (−1)	7.87 (−1)
22.00	1.20 (+0)	1.26 (+0)	1.29 (+0)	1.31 (+0)	1.32 (+0)	1.33 (+0)
22.33	1.99 (+0)	2.11 (+0)	2.17 (+0)	2.20 (+0)	2.24 (+0)	2.26 (+0)
22.67	3.27 (+0)	3.54 (+0)	3.65 (+0)	3.71 (+0)	3.76 (+0)	3.76 (+0)
23.00	5.18 (+0)	5.82 (+0)	6.11 (+0)	6.26 (+0)	6.37 (+0)	6.37 (+0)
23.33	8.11 (+0)	9.49 (+0)	1.01 (+1)	1.05 (+1)	1.08 (+1)	1.08 (+1)
23.67	1.25 (+1)	1.51 (+1)	1.64 (+1)	1.72 (+1)	1.80 (+1)	1.83 (+1)
24.00	—	2.36 (+1)	2.63 (+1)	2.79 (+1)	2.95 (+1)	3.02 (+1)
24.33	—	3.56 (+1)	4.09 (+1)	4.42 (+1)	4.77 (+1)	4.93 (+1)
24.67	—	—	6.21 (+1)	6.81 (+1)	7.56 (+1)	7.99 (+1)

The notation '1.27 (−3)' has been used to represent 1.27×10^{-3}.

Table 33. FWHM of Balmer-γ (in nm). $\mu = 1$.

log(N_e) (m^{-3})	Temperature (K)					
	5000	10 000	15 000	20 000	30 000	40 000
20.00	5.70 (−2)	5.93 (−2)	5.99 (−2)	5.98 (−2)	5.91 (−2)	5.81 (−2)
20.33	9.35 (−2)	9.80 (−2)	9.95 (−2)	9.99 (−2)	9.97 (−2)	9.89 (−2)
20.67	1.56 (−1)	1.61 (−1)	1.63 (−1)	1.64 (−1)	1.66 (−1)	1.67 (−1)
21.00	2.60 (−1)	2.71 (−1)	2.75 (−1)	2.78 (−1)	2.80 (−1)	2.80 (−1)
21.33	4.32 (−1)	4.50 (−1)	4.58 (−1)	4.63 (−1)	4.67 (−1)	4.69 (−1)
21.67	7.20 (−1)	7.49 (−1)	7.62 (−1)	7.70 (−1)	7.79 (−1)	7.82 (−1)
22.00	1.19 (+0)	1.26 (+0)	1.29 (+0)	1.30 (+0)	1.32 (+0)	1.32 (+0)
22.33	1.99 (+0)	2.11 (+0)	2.16 (+0)	2.20 (+0)	2.23 (+0)	2.25 (+0)
22.67	3.26 (+0)	3.53 (+0)	3.64 (+0)	3.70 (+0)	3.75 (+0)	3.75 (+0)
23.00	5.17 (+0)	5.82 (+0)	6.11 (+0)	6.25 (+0)	6.36 (+0)	6.35 (+0)
23.33	8.11 (+0)	9.48 (+0)	1.01 (+1)	1.05 (+1)	1.08 (+1)	1.08 (+1)
23.67	1.25 (+1)	1.51 (+1)	1.64 (+1)	1.72 (+1)	1.80 (+1)	1.83 (+1)
24.00	—	2.36 (+1)	2.62 (+1)	2.78 (+1)	2.95 (+1)	3.01 (+1)
24.33	—	3.56 (+1)	4.08 (+1)	4.41 (+1)	4.77 (+1)	4.93 (+1)
24.67	—	—	6.20 (+1)	6.81 (+1)	7.56 (+1)	7.99 (+1)

The notation '1.27 (−3)' has been used to represent 1.27×10^{-3}.

trying to derive new width values from the data appearing in the tables, specially as far as temperature is concerned.

4.1. Lyman-α

Tables 5–9 show the results of the simulations for the full width at half height of the Lyman alpha line as a function of the electron density and the temperature for different values of the reduced mass μ. As a consequence of the high computational cost of the low-density cases for this spectral line, the lowest value of N_e was 10^{21} m^{-3}. In fact, this line was

Table 34. FWHM of Balmer-γ (in nm). $\mu = 2$.

log(N_e) (m^{-3})	Temperature (K)					
	5000	10 000	15 000	20 000	30 000	40 000
20.00	5.44 (−2)	5.76 (−2)	5.87 (−2)	5.91 (−2)	5.91 (−2)	5.86 (−2)
20.33	8.84 (−2)	9.39 (−2)	9.62 (−2)	9.74 (−2)	9.85 (−2)	9.88 (−2)
20.67	1.48 (−1)	1.53 (−1)	1.56 (−1)	1.58 (−1)	1.61 (−1)	1.64 (−1)
21.00	2.49 (−1)	2.58 (−1)	2.63 (−1)	2.66 (−1)	2.70 (−1)	2.72 (−1)
21.33	4.15 (−1)	4.29 (−1)	4.36 (−1)	4.41 (−1)	4.47 (−1)	4.51 (−1)
21.67	7.02 (−1)	7.21 (−1)	7.31 (−1)	7.38 (−1)	7.46 (−1)	7.50 (−1)
22.00	1.18 (+0)	1.22 (+0)	1.25 (+0)	1.26 (+0)	1.27 (+0)	1.27 (+0)
22.33	1.97 (+0)	2.07 (+0)	2.12 (+0)	2.14 (+0)	2.17 (+0)	2.18 (+0)
22.67	3.24 (+0)	3.49 (+0)	3.60 (+0)	3.65 (+0)	3.67 (+0)	3.65 (+0)
23.00	5.15 (+0)	5.76 (+0)	6.02 (+0)	6.16 (+0)	6.24 (+0)	6.22 (+0)
23.33	8.08 (+0)	9.41 (+0)	1.00 (+1)	1.04 (+1)	1.06 (+1)	1.07 (+1)
23.67	1.24 (+1)	1.50 (+1)	1.64 (+1)	1.71 (+1)	1.78 (+1)	1.81 (+1)
24.00	—	2.35 (+1)	2.61 (+1)	2.77 (+1)	2.93 (+1)	3.00 (+1)
24.33	—	3.54 (+1)	4.07 (+1)	4.40 (+1)	4.76 (+1)	4.92 (+1)
24.67	—	—	6.18 (+1)	6.79 (+1)	7.54 (+1)	7.96 (+1)

The notation '1.27 (−3)' has been used to represent 1.27×10^{-3}.

calculated just in the conditions of the simulations of series 1—see table 2. On the other hand, calculations of this line for lower densities would not make too much sense unless the fine-structure effects were included too.

The fact that Lyman-α is made of a strong central component between two weaker ones, makes it the most sensitive to the ion dynamics effects among the lines presented in this work. As previously pointed out, the relevance of this mechanism and its dependence on the reduced mass or the temperature change with the plasma conditions. At very low densities and high temperatures, the ion dynamics effect will show all the characteristics of an impact-broadening mechanism: the line width will increase with μ and decrease with T. This is shown by figure 2, where the plot reveals how the width grows as μ increases. However, as the density goes up, this trend inverts itself. In particular, for the extreme cases represented in figure 2, δ goes from 0.2 at $\mu = 0.5$, $N_e = 10^{21}$, $T = 20\,200$ K to 0.8 at $\mu = 2$, $N_e = 10^{22.7}$, $T = 72\,600$ K. On the other hand, figure 3 illustrates that when the temperature is not too high, the ion dynamics effect does not have an impact nature, even for low densities. In figure 3, the lowest δ value is 0.65. Figure 4 shows the dependence of the width on the reduced mass for different values of the electronic density and a fixed temperature.

The behaviour of the width as a function of plasma temperature is well illustrated in figure 5. The change of trend caused by the transition from the impact to the dynamic regime is very clearly seen here. In fact, the width has been plotted on a $\Delta\Omega$ scale, in order to leave out all the dominant contributions tied to the quasistatic fields statistics. It can be observed how, at low densities, if the temperature is not very high, the width decreases when the reduced mass of the emitter–perturber pair grows. When the temperature exceeds certain values, this trend inverts and the ion impact regime is entered. This situation is not seen at high densities within the temperature range covered in the simulations. Still for figure 5, in the case $N_e = 10^{23}$ m^{-3} and high temperatures a growing trend is observed in the width as a function of T, specially when μ is small; this clearly manifests that the zone of dominance of ion dynamics broadening has been reached: width grows with temperature
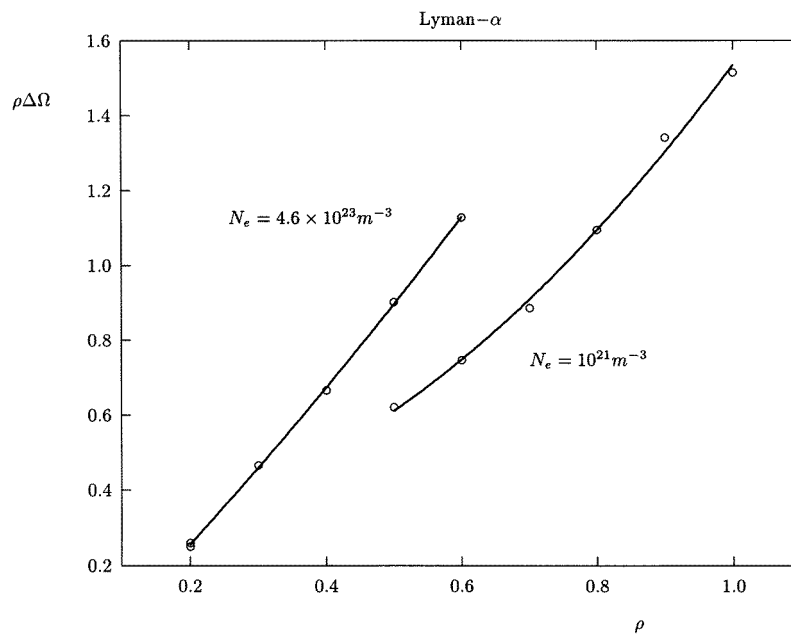
Figure 1. Sample plot of the smoothing of the raw data caused by the fit of the width of the Lyman-α line normalized according to the expression (40). $\mu = 0.5$ in this case.
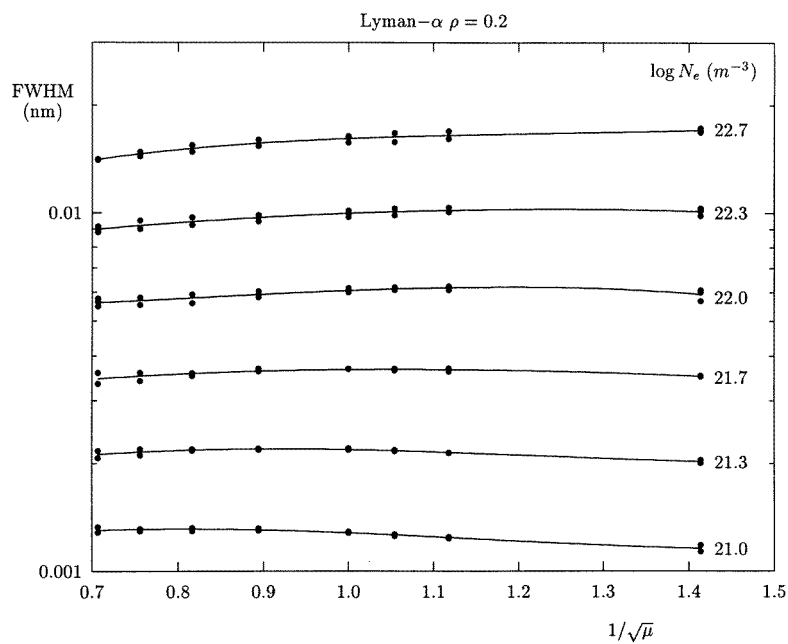
Figure 2. Lyman-α: FWHM as a function of the reduced mass. The dots correspond with the three simulated cases for 100, 500 and 2700 particles. The solid curves are the least-square fitting to a degree 3 polynomial of the form $\Delta\lambda_{1/2} = P_3(1/\sqrt{\mu})$ for every value of N_e. Although they are represented as a log plot, the fittings were carried out on a linear scale. $\rho = 0.2$.
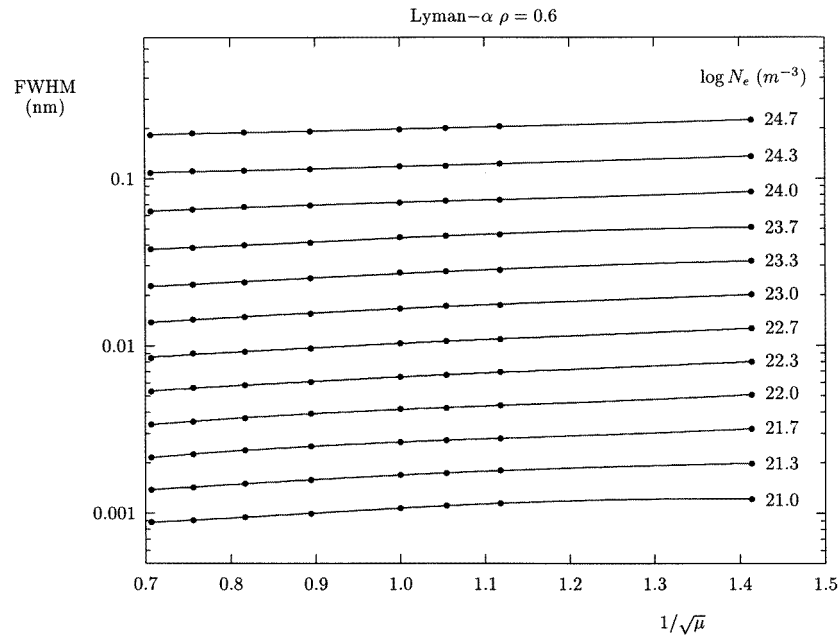
Figure 3. Lyman-α: FWHM as a function of the reduced mass. $\rho = 0.6$.
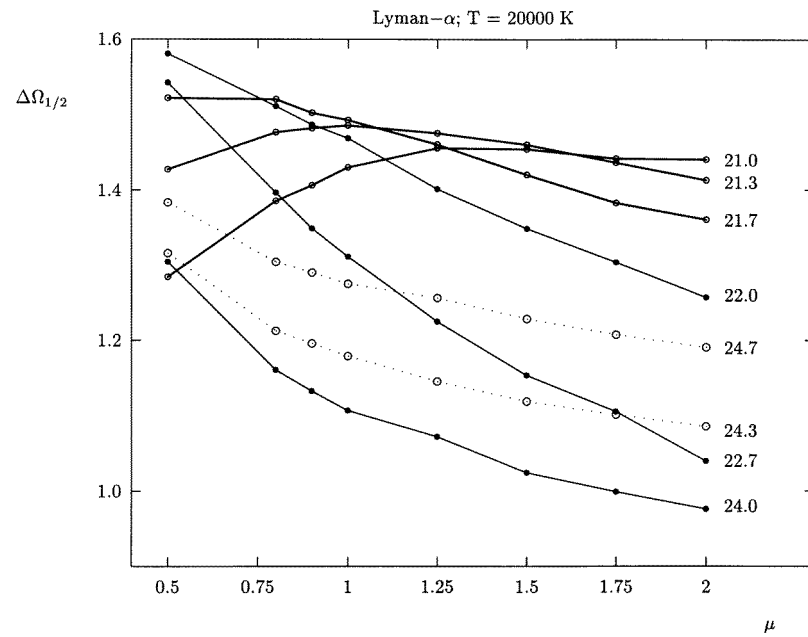
Figure 4. Lyman-α: FWHM as a function of the electron density and the reduced mass. $\Delta\Omega$ scale was used for the width. $T = 20\,000$ K. Numerical values beside each plot give the decimal logarithm of the electron density in units of m^{-3}.
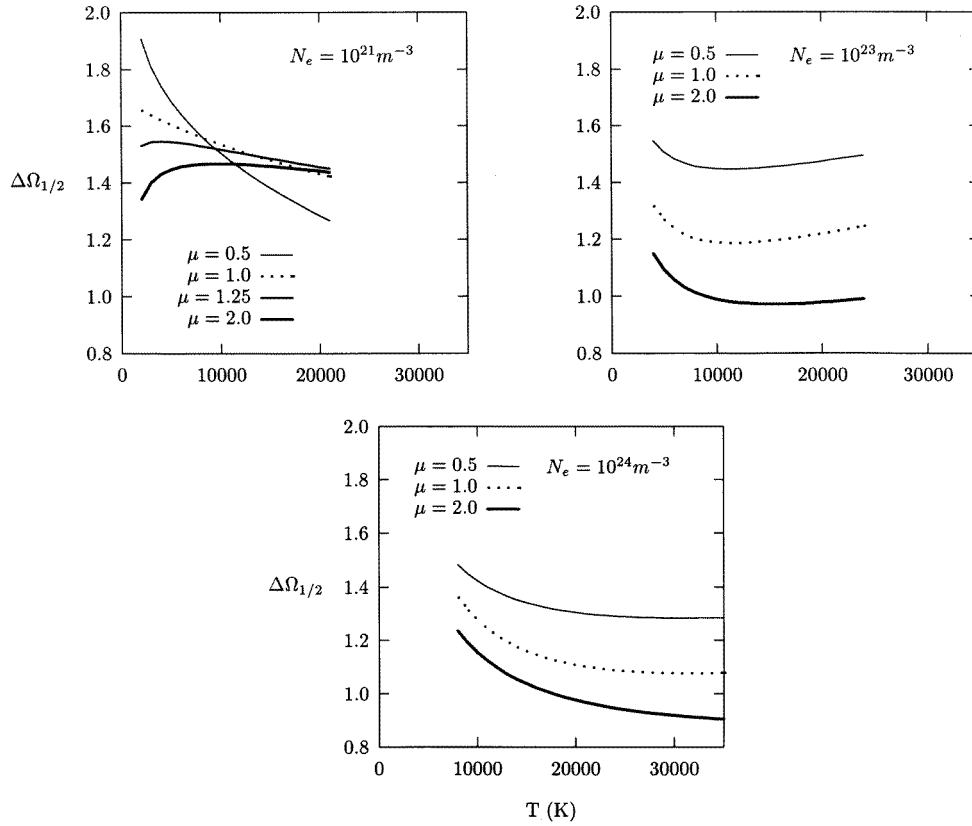
Figure 5. Lyman-α: FWHM as a function of the temperature for different values of N_e and μ. $\Delta\Omega$ scale was again used for the widths.

and decreases with μ. As the density increases, and the line width with it, the ion dynamics effects progressively lose relevance since the correlation time of the emission process is so drastically reduced that there is no place for significant changes of the ion microfield. In fact, the plots in figure 5 show that at very high densities and very low temperatures, ion dynamics effects are of little importance and the temperature dependence is given by the characteristic decreasing pattern of the electron impact. As T grows, ion dynamics regains importance—see how the three curves for $N_e = 10^{24}$ m^{-3} separate from each other—and can compensate the temperature dependence ascribed to the electron impact effect.

Finally, figure 6 is shown as a last illustration of the functional dependences of the ion dynamics width on the plasma parameters. To construct this graph, a least-squares fit of the form $\Delta\Omega_{1/2} = a + b/\sqrt{\mu}$ for the line width in every temperature and density condition has been made first. This gives an idea about the *average* trends for all the values of μ included in each case. Obviously this fit cannot properly reflect the functional dependence of the width on the reduced mass in the transition region between the impact and dynamic broadening regimes but fills the gap to get an overall idea of the phenomenon. Then, the value of the slope of these fittings, b, as a function of plasma temperature has finally been plotted in the figure. At low densities, this slope decreases with temperature until it becomes negative if T is high enough—ion impact domain. At high densities, the influence of the effects of ion motion increases with temperature.
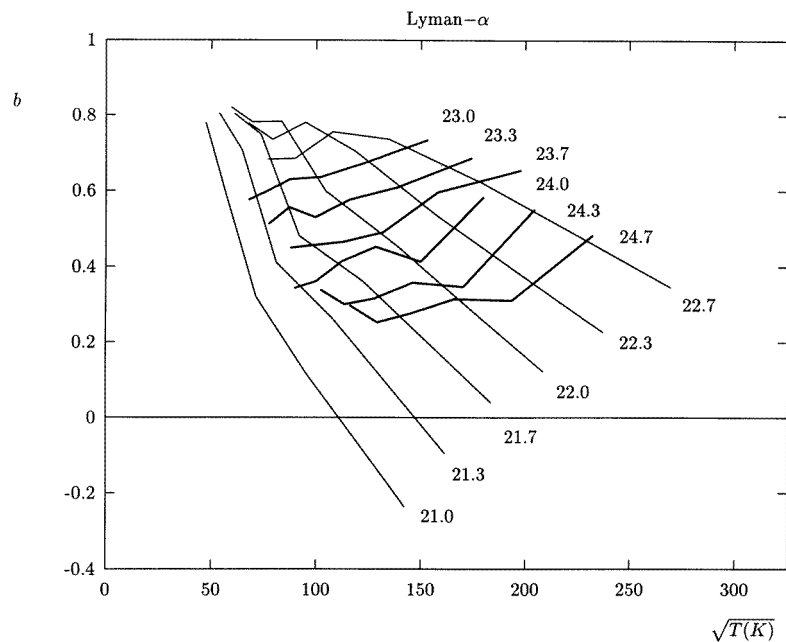
Figure 6. Lyman-α: plot of b in the expression $\Delta\Omega_{1/2} = a + b/\sqrt{\mu}$ as a function of the electron density and the temperature. As usual, the numbers give the log value of the density.
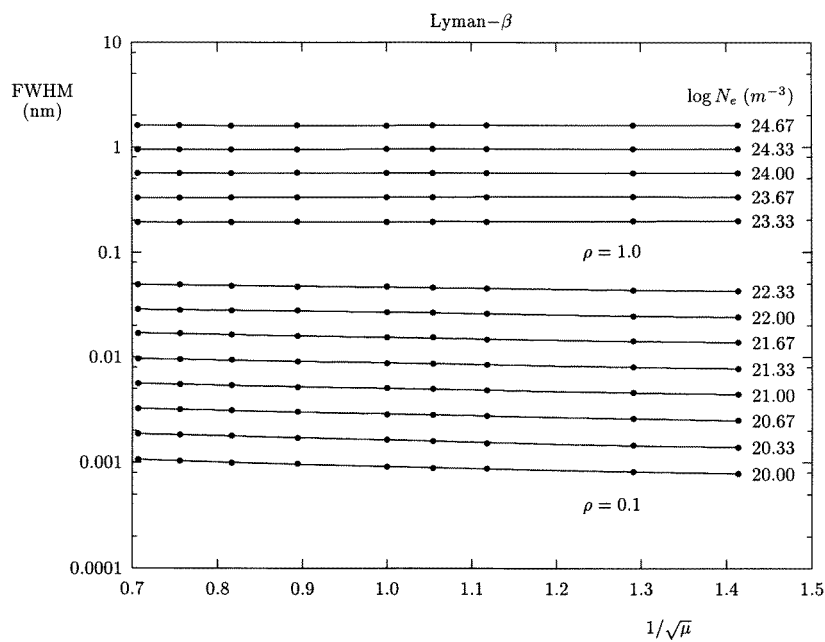
Figure 7. Lyman-β: FWHM as a function of the reduced mass. Notation as in figure 2.
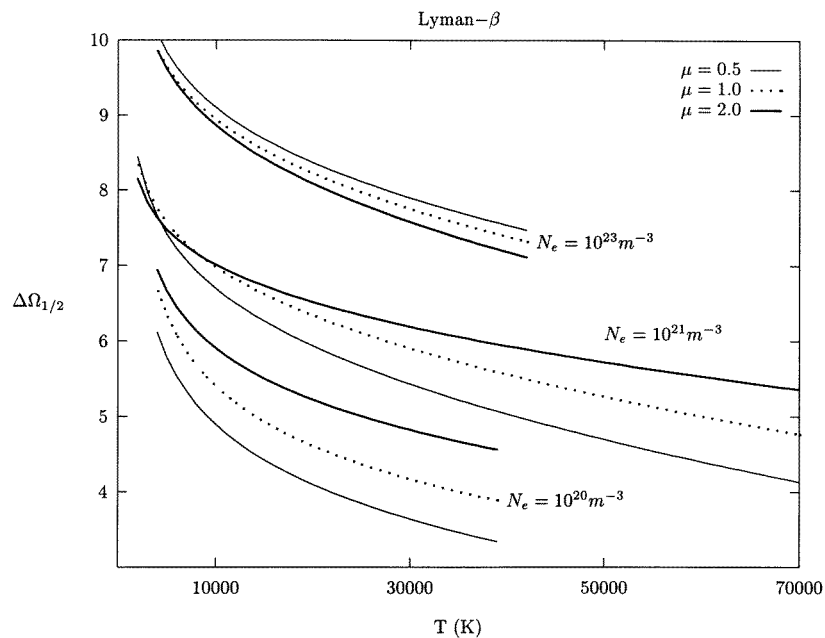
Figure 8. Lyman-β: FWHM in $\Delta\Omega$ scale as a function of the temperature for different values of N_e and μ.
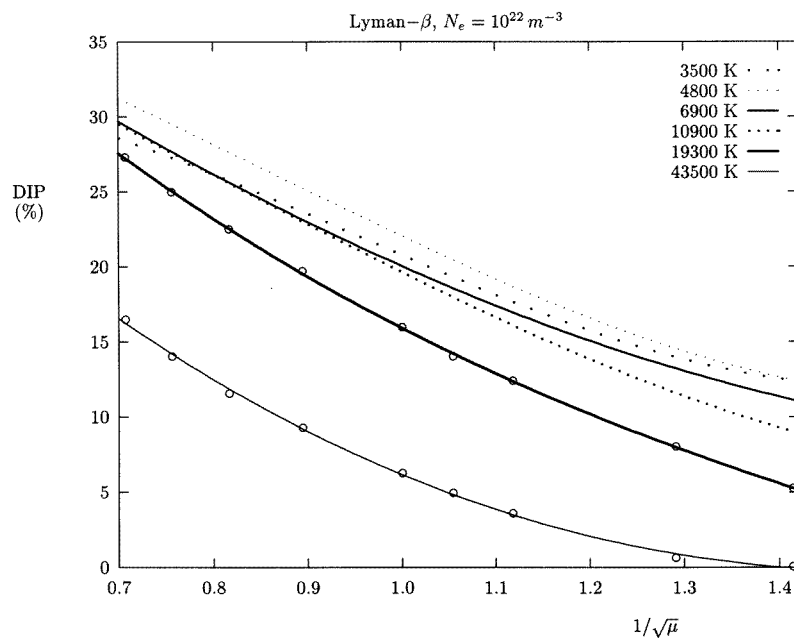

Figure 9. Lyman-β: central dip (%) as a function of the reduced mass for different T values. The curves represent the fittings of the simulation points, which have been excluded in some cases to avoid confusion. The dispersion in these omitted cases is similar to the ones presented in the graph. $N_e = 10^{22}$ m^{-3} in all cases.
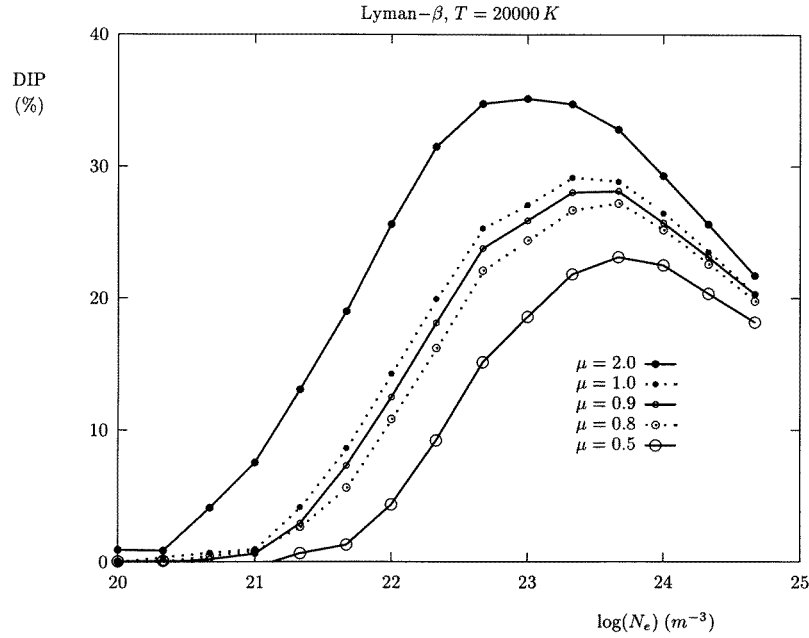
Figure 10. Lyman-β: central dip (%) as a function of the electron density for different values of the reduced mass. $T = 20\,000$ K in all cases.

The comparison of our results both with the experimental data and those of other authors is summarized in table 3, which contains the results of the experiment of Grützmacher and Wende [38] for a H + Ar$^+$ plasma ($\mu = 0.975$).

4.2. Lyman-β

The width of the Lyman-β line is less sensitive to the ion dynamics effects than the Lyman-α as a consequence of the lack of a central component without Stark shift. However, and from a qualitative point of view, every comment made about the width of Lyman-α also applies here. Figure 7 gives account of the behaviour of the width as a function of the reduced mass μ in the two extreme cases of ρ considered in this work. The effects of ion dynamics are more clearly seen at low densities and high temperatures. Figure 8 shows this fact: an ion impact broadening is seen at low densities and high temperatures—since the width grows with the reduced mass. At high densities, the dynamic broadening mechanism appears and the dependence on μ inverts. It can also be seen in figure 8 that the influence of ion dynamics effects on the line width quickly decreases as the density grows.

Certainly, the central dip of the line is the zone of the profile most affected by the movement of the heavy perturbers. Qualitative analysis of the influence of ion movement on this parameter is much more complicated than for the line width. This is a consequence of the particularities of the influence of the electronic density: when it is low, the Stark components will be very close together and their overlapping will make the dip disappear, whilst, when density gets higher, the impact width of every component is also high and thus its width increases, which makes the dip smaller once more when they overlap. So, there is a certain density range where this dip can be clearly observed and in this range the effects of ion dynamics show the typical dynamic broadening characteristics, that is to
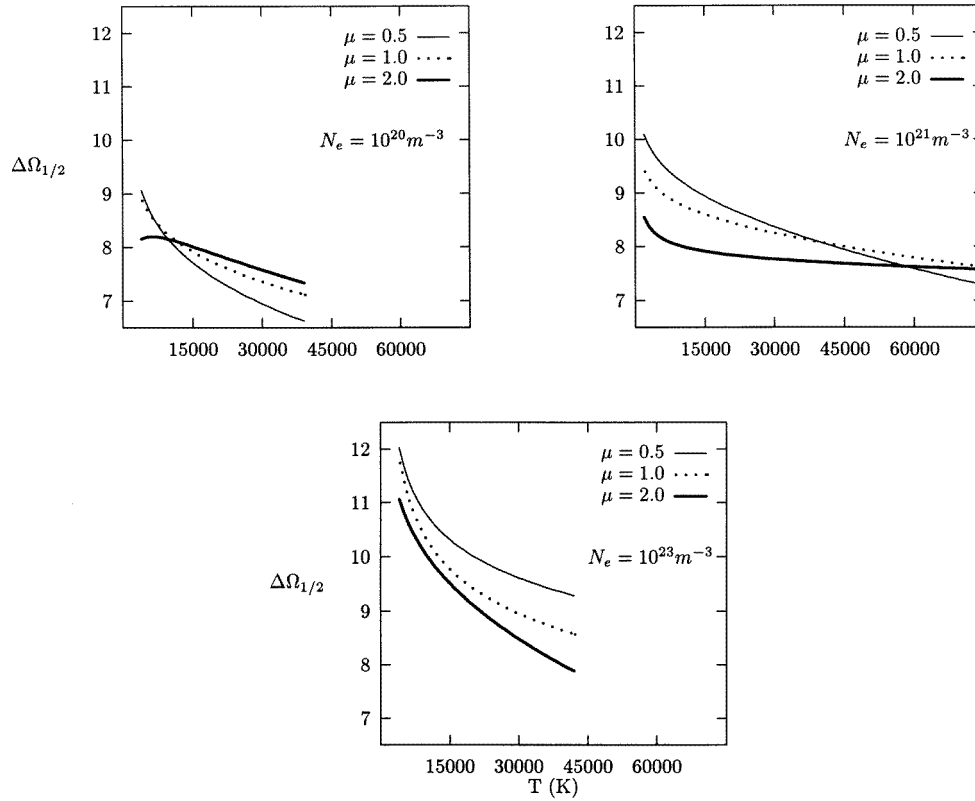
Figure 11. Lyman-γ: FWHM in $\Delta\Omega$ scale as a function of the temperature for different values of N_e and μ.

say a $\sqrt{T/\mu}$ dependence. So that, in general, it can be seen that as μ grows the central dip does also, and vice versa with the temperature. Figure 9 illustrates this kind of typical behaviour of the central dip of the line—defined as the ratio $(I_{max} - I(0))/I_{max}$—for a given electronic density. The dependence of the dip on the electronic density itself is illustrated in figure 10.

Numerical results of the full width at half height of Lyman-β are presented in tables 10–14.

4.3. Lyman-γ

The shape of this spectral line, specially at its centre, is given by the presence of a central component without Stark shift surrounded by much less intense side components. The influence of the ion dynamics effects on the line width attain to the broadening of that central component which causes a reduction of height both of this component and of the line as a whole. This makes the total width too dependent on the behaviour of its central component and, as a consequence, the noise level of the simulation results is higher for this line. Figure 11 shows this phenomenon as a function of the reduced mass and the temperature for different values of the electronic density.

The behaviour of the width of the central component is specially noticed by the reduction of the characteristic lateral shoulder of the line. In this way, the relation between the width
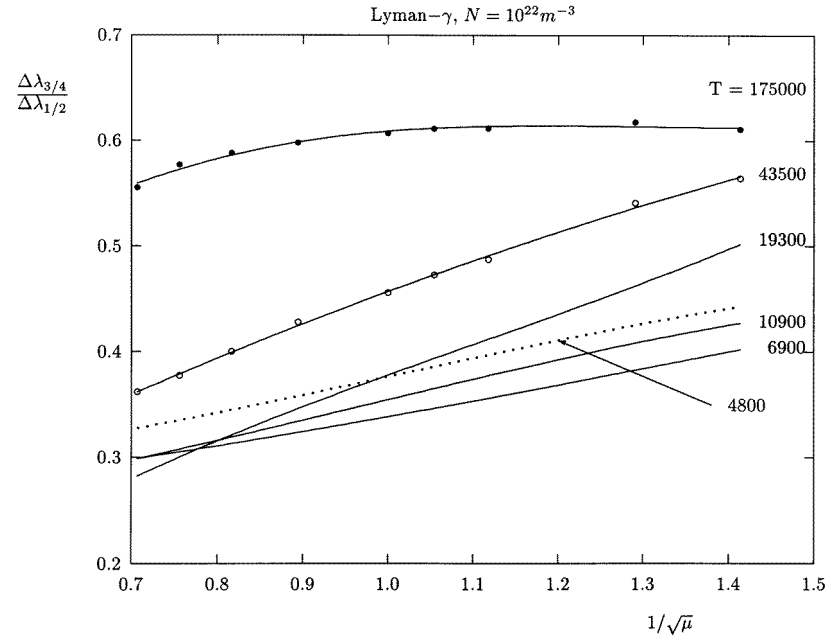
Figure 12. Lyman-γ: $\Delta\lambda_{3/4}/\Delta\lambda_{1/2}$ as a function of the reduced mass for different temperature values. $N_e = 10^{22}$ m^{-3} in all cases.
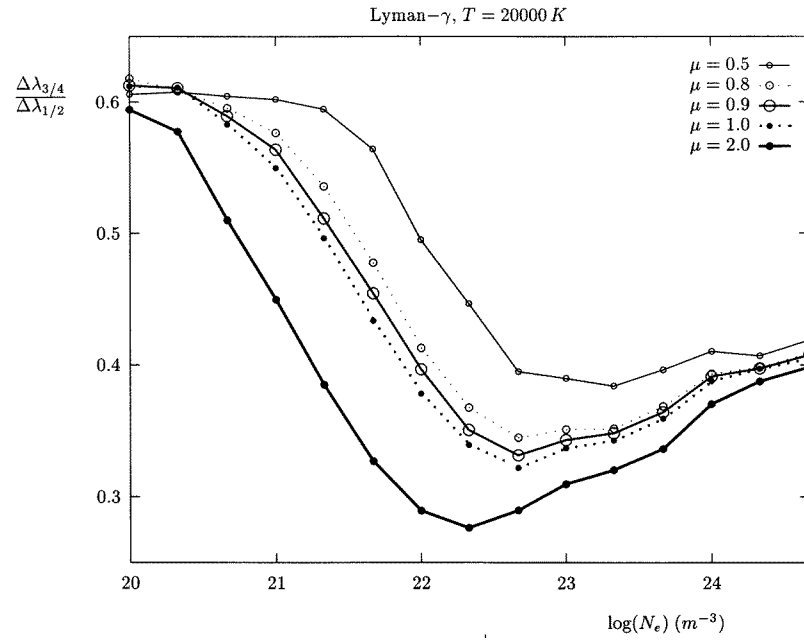
Figure 13. Lyman-γ: $\Delta\lambda_{3/4}/\Delta\lambda_{1/2}$ as a function of the electronic density for different μ values. $T = 20\,000$ K in all cases.
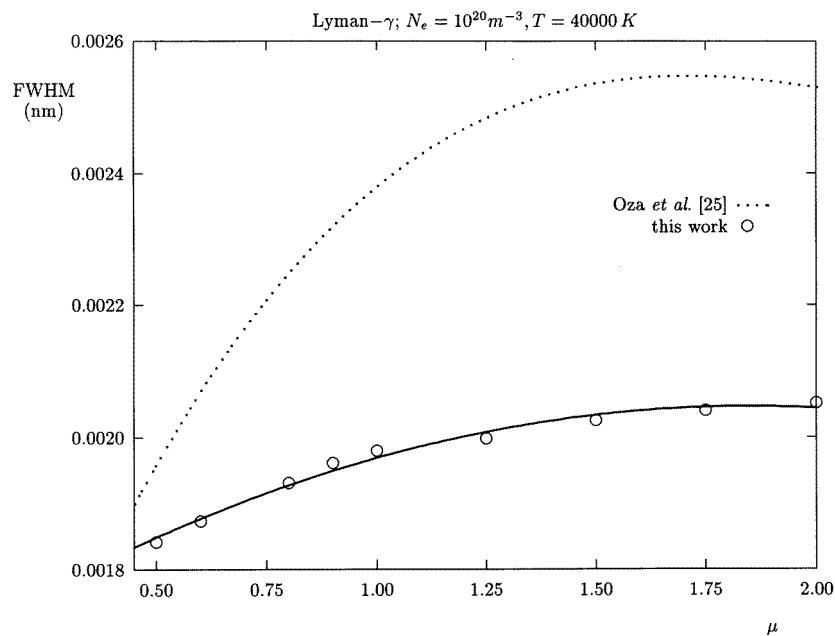
Figure 14. Lyman-γ: FWHM versus reduced mass μ, low densities. The results in this work are compared with the semianalytical calculations of Oza *et al* [25]. Low-density range.
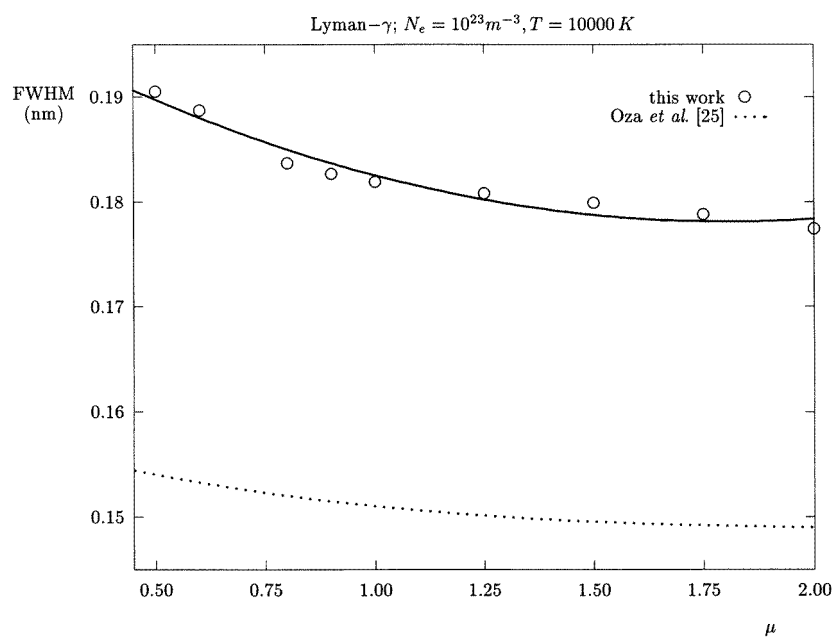
Figure 15. Lyman-γ: FWHM versus reduced mass μ, high densities. The results in this work are compared with the semianalytical calculations of Oza *et al* [25].
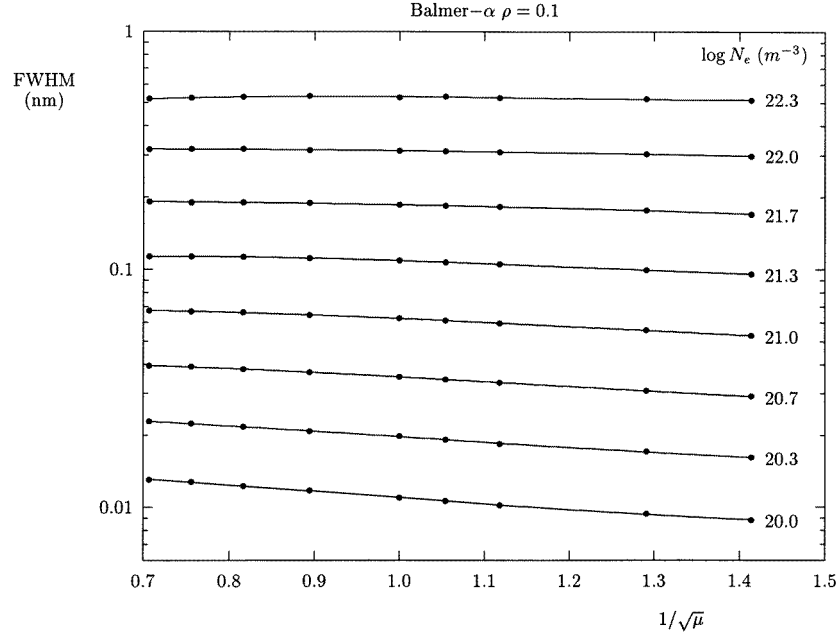
Figure 16. Balmer-α: FWHM versus reduced mass μ. $\rho = 0.1$.

at three quarters and at half height is highly sensitive to the effects of ion motion. This ratio gives information about the relation between the broadening of the central component and that of the complete line. The comments made about the central dip of the Lyman-β line would apply here too.

Figure 12 shows the usual dependence of this parameter on the reduced mass. Similar behaviour is found for other density conditions. Figure 13 shows the dependence of this parameter on the density of perturbers and the reduced mass for a given temperature.

There are few experimental data for the Lyman-γ line. As a comparison with the experiments, a reference to [39] is significant. There, one finds that for plasma conditions of $N_e = 2 \times 10^{23}$ m^{-3}, $T = 15\,500$ K, $\mu = 0.975$, the total experimental width is 0.29 nm and the relation $\Delta\lambda_{3/4}/\Delta\lambda_{1/2} = 0.41$. The simulation results for the same conditions are 0.305 nm and 0.352, respectively. The Doppler width for this case would be around 8.7×10^{-3} nm. Further comparison of our simulation results with the semianalytical calculations of Oza *et al* [25] show noticeable discrepancies, as can be seen in figures 14 and 15. Until this paper, the reason for this was not obvious to us.

Numerical results of the full width at half height of Lyman-γ are presented in tables 15–19.

4.4. Balmer-α

Although this line lays inside the visible part of the spectrum and this should make it a suitable candidate for diagnostic purposes, its use has not been widespread because of three fundamental reasons: it shows high self-absorption levels, it is in a zone of the spectrum where a great number of lines of other elements blur the shape of the line and, finally, the theoretical predictions of the lineshape do not agree well enough with the experiments. The latter has become less important as the numerical calculations began to include ion-
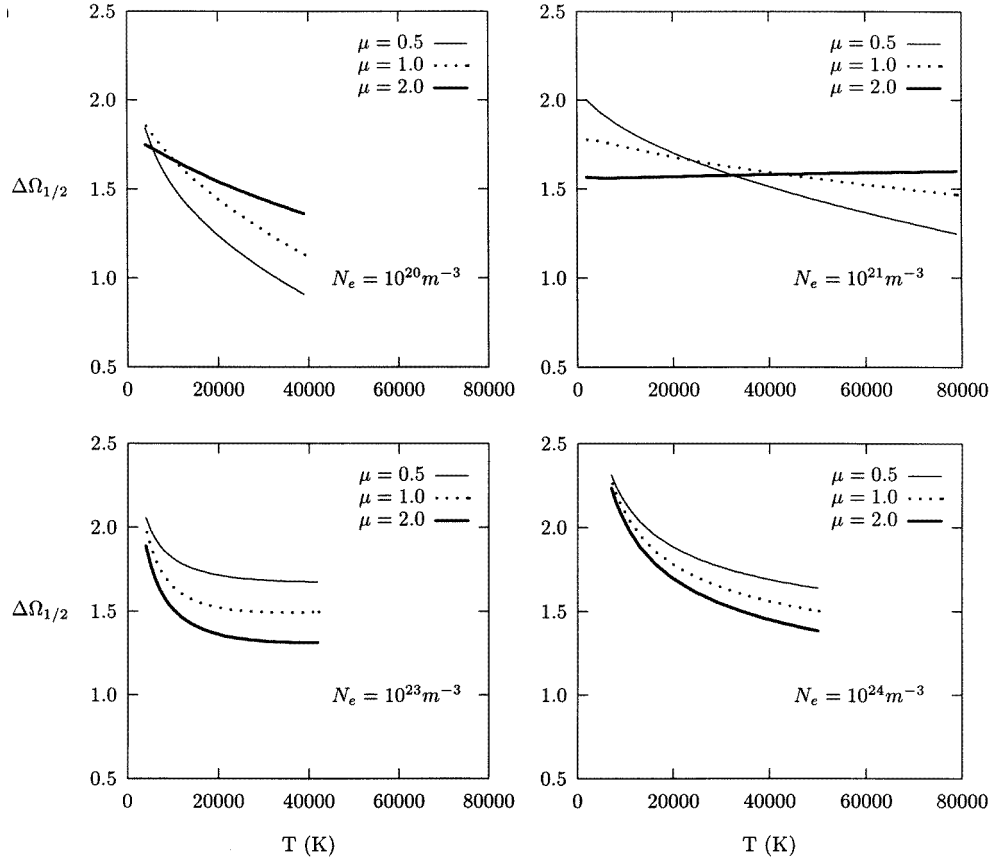
Figure 17. Balmer-α: FWHM in units of $\Delta\Omega$ as a function of temperature for different values of N_e and μ.

dynamics effects, which reveal themselves as very important in this line. For some time, Balmer-α has had increased relevance in plasma diagnosis as a consequence of the growing interest in opacity measures of stellar atmospheres.

Although at a smaller scale, ion dynamics effects show up in pretty much the same way as in Lyman-α as a consequence of a similar lineshape, namely, the experimental width is notably higher than predicted by the theories which do not take ion dynamics into account. At $N_e = 10^{21}$ m^{-3} and $T = 40\,000$ K, the 0.011 nm of Griem's calculations [2] or the 0.0093 nm of VCS [1] contrast with the results obtained in the simulations: 0.067 nm for a plasma of $\mu = 1$ and 0.064 nm for a pure hydrogen one. Around these plasma conditions, the width of the line shows a characteristic ion-impact behaviour with respect to the reduced mass and the temperature—see figures 16 and 17 and their similarity with the ones of Lyman-α. In fact, the comparison of our simulation results with the ones carried out by Stehlé [40] under a framework in which the effect of ion dynamics is considered as an impact phenomenon, shows an excellent agreement in quite a wide range—see figure 18.

Figure 19, similar to figure 6, illustrates the global behaviour of the line width as a function of the reduced mass of the heavy perturbers and the temperature in a wide range of electron densities. Qualitatively, a very similar result to the Lyman-α case is obtained.

The comparison of the simulation results with the ones of the experiments in the

Balmer−α; T = 40000 K
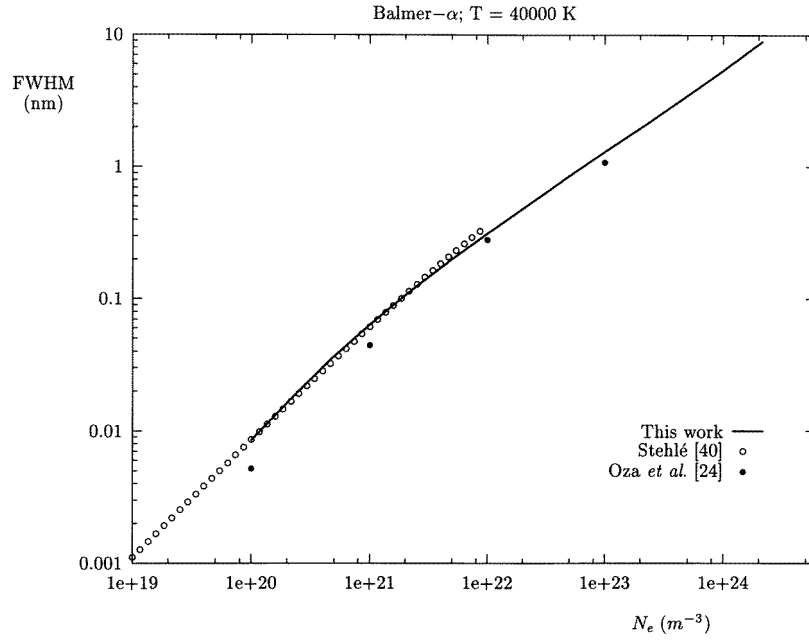
Figure 18. Balmer-α: FWHM in a H–H$^+$ plasma as a function of the electron density. The dotted curve represents the ion-impact broadening given by the corresponding analytical expression found in [40].
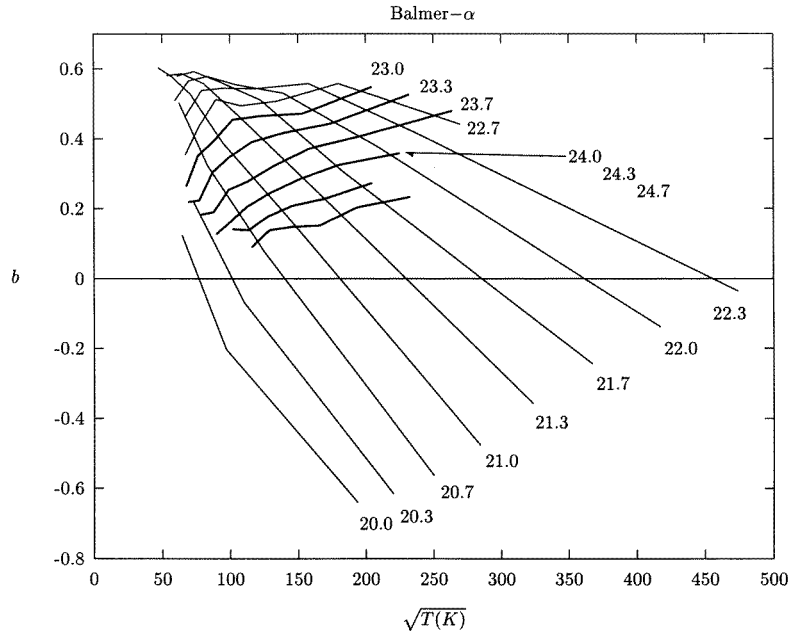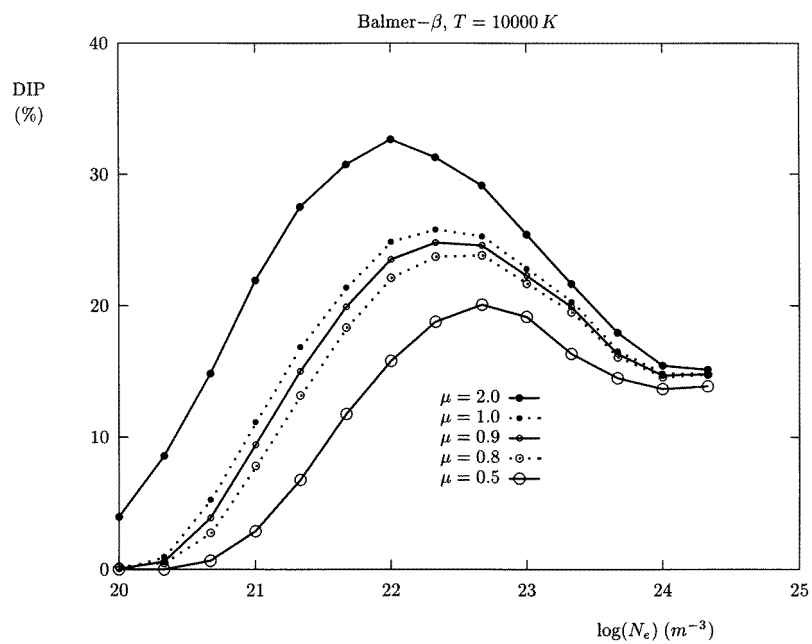
Balmer−α

Figure 19. Balmer-α: plot of b in the expression $\Delta\Omega_{1/2} = a + b/\sqrt{\mu}$ as a function of the electron density and the temperature. The numbers beside the curves show the log value of the density.
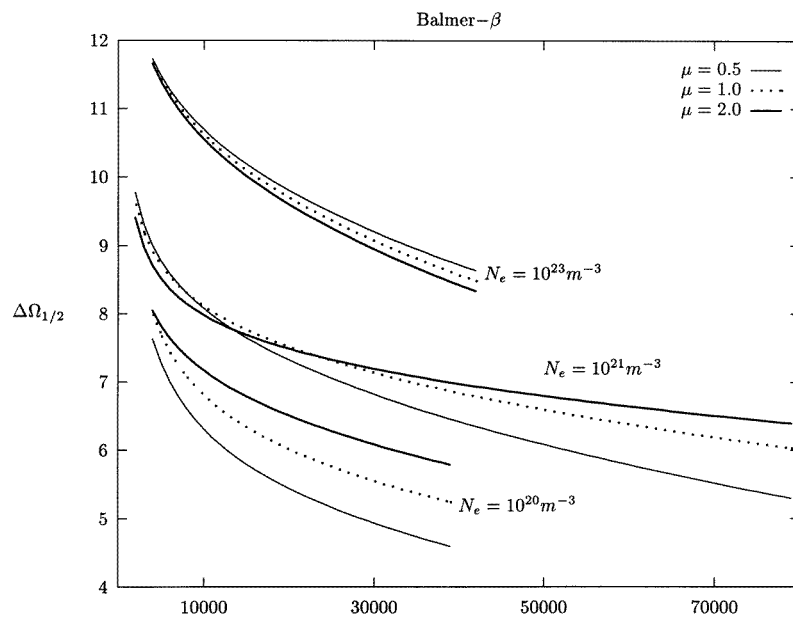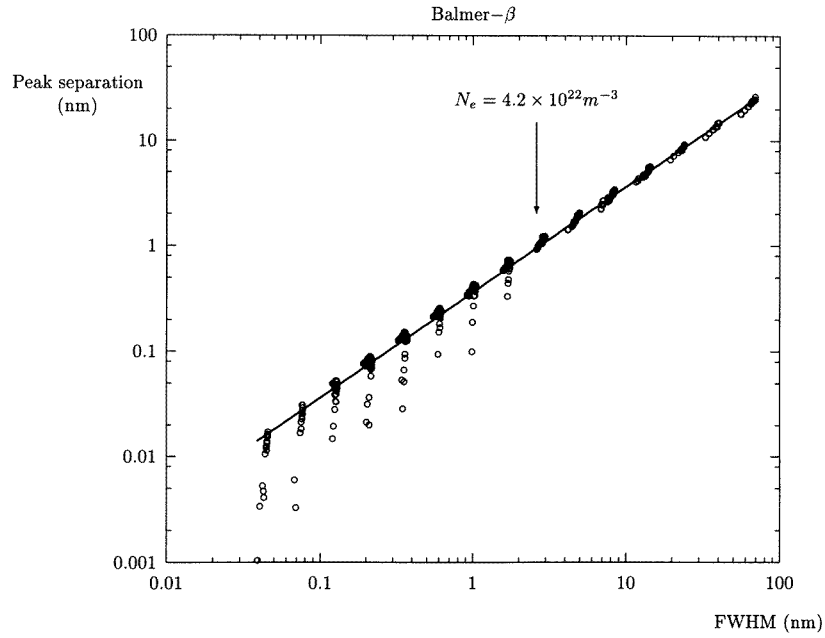
Figure 20. Balmer-β: FWHM in $\Delta\Omega$ units as a function of temperature for different values of N_e and μ.
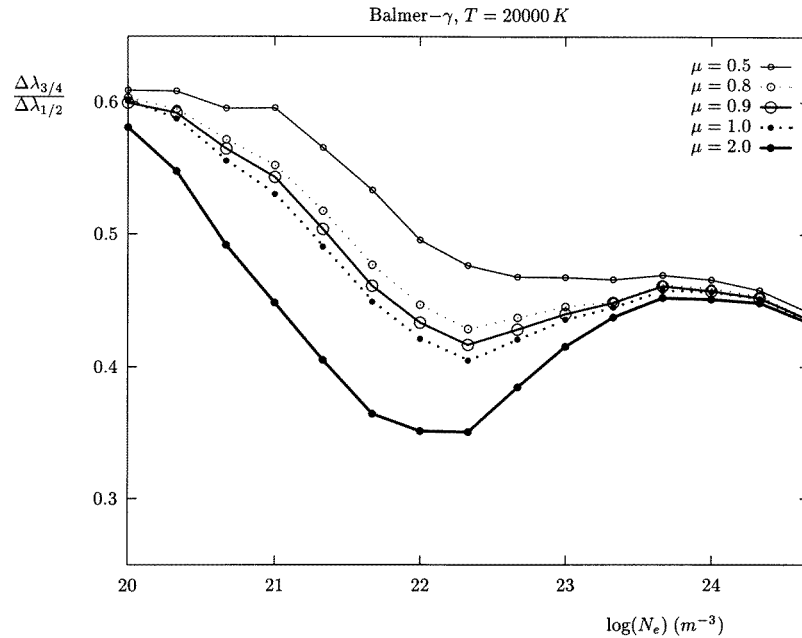

Figure 21. Balmer-β: central dip (%) as a function of the electron density for different values of the reduced mass. $T = 10\,000$ K in all cases.

Balmer$-\beta$

Figure 22. Balmer-β: peak separation as a function of FWHM. The points represent all the values obtained directly from the simulation, which includes different ρ, N_e, T and μ. The full line represents the mean value of the quotients (peak separation)/FWHM using all the data for $N_e \geqslant 4 \times 10^{22}$ m^{-3}. The quotient value is 0.362.
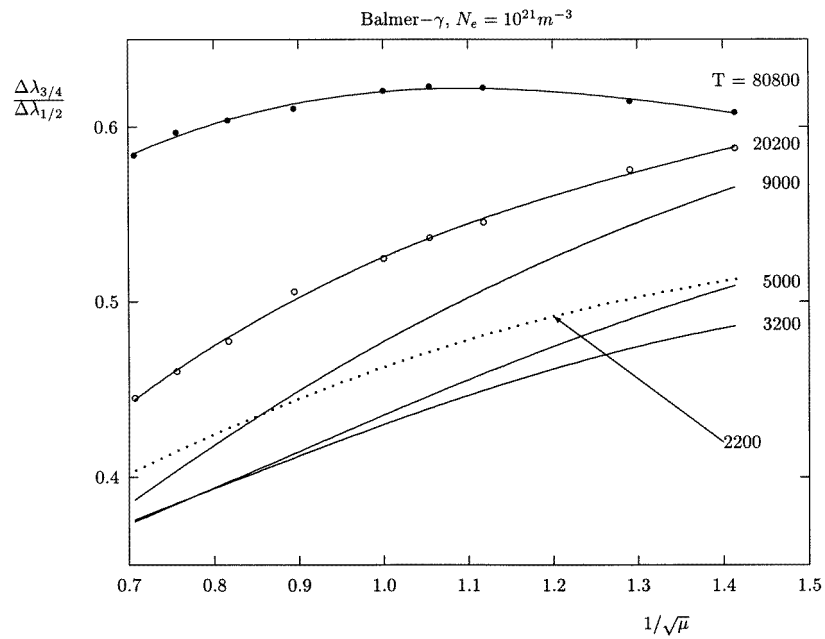
Balmer$-\gamma$, $N_e = 10^{21}m^{-3}$

Figure 23. Balmer-γ: $\Delta\lambda_{3/4}/\Delta\lambda_{1/2}$ as a function of the reduced mass μ for different temperature values. $\log(N_e \ [\mathrm{m}^{-3}]) = 21.33$ in all cases.

Balmer−γ, $T = 20000\,K$

Figure 24. Balmer-γ: $\Delta\lambda_{3/4}/\Delta\lambda_{1/2}$ as a function of the electron density for different values of the reduced mass μ. $T = 20\,000$ K in all cases.

bibliography is specially noticeable in this line—see table 4, which includes highly disperse results and very low density measurements. In this range, the fine-structure effects clearly arise: the fine structure originates a doublet which peak separation is 0.015 nm. Weber's experimental result is very close to the simple overlapping of the two contributions. See also the comment in [46] about the work of Vitel [45].

Tables 20–24 present useful results for plasma diagnosis using this line.

4.5. Balmer-β

This line comes to be the most widely used for diagnosis purposes because of its great Stark width and the lack of the disadvantages of Balmer-α: it is relatively isolated at its spectral range, it has no significant self-absorption and, since its width is almost independent of the plasma temperature and the ion dynamics effects, the results of the conventional theoretical models are really accurate.

The influence of the perturbers mass can be observed in figure 20. There it may be seen how the dependence of the full width on μ and T is qualitatively similar to that in other spectral lines although it is quantitatively less apparent than in, for example, Balmer-α (cf figure 17).

As in Lyman-β, the influence of the reduced mass of the emitter–perturber pair is most clear at the central dip. As seen in figure 21, the dependence of this dip with the electron density and the mass of the perturbers is very similar to that in the former line.

The peak separation may be a relatively good diagnosis parameter in this line, specially for high-density conditions (above 10^{22} m^{-3}). Balmer-β appears very often in multichannel spectra registered with a window not so wide as to embrace the complete profile but enough to cover the peak-to-peak distance. Figure 22 shows the relation between this distance and

the full width at half maximum (FWHM). At high densities, when that separation grows, the ratio remains almost a constant and it is thus a very useful parameter for diagnosis. Taking into account only the cases $N_e \geqslant 4 \times 10^{22}$ m^{-3}, a ratio (peak separation)/FWHM of 0.36 ± 0.02 has been obtained with the calculations of this work. Helbig and Nick [47] found an experimental value of 0.354 ± 0.011, very similar to the one of Wiese (0.36) cited in the same paper. The calculations by Vidal *et al* give a value of 0.37 and Seidel's MMM 0.349.

4.6. Balmer-γ

Like Balmer-β, the width of this line is quite insensitive to ion dynamics effects relative to its absolute value (up to 6%). As in Lyman-γ, only the central structure of the line is affected by ion movement and similar comments to the ones on that line apply. The three-quarters to one-half width ratio is influenced by ion dynamics as it is shown in figures 23 and 24. The dependence of the lineshape the plasma density and temperature is qualitatively similar to that of Lyman-γ.

Acknowledgments

Appendix. Lyman-γ autocorrelation function

In the following expression, which gives the Lyman-γ autocorrelation function, the notation $[\![\alpha_0; \boldsymbol{\alpha}]\!]$ has been used to represent the solution of equation (13) with positive sign in χ and $[\![\beta_0; \boldsymbol{\beta}]\!]$ for the negative-sign solution.

$$C_{\text{lyman}-\gamma}(t) = \tfrac{2}{30}\{\alpha_0\beta_0[15 - 30(\alpha^2 + \beta^2) + 54\alpha^2\beta^2 + 18(\boldsymbol{\alpha} \cdot \boldsymbol{\beta})^2]$$
$$+ (\boldsymbol{\alpha} \cdot \boldsymbol{\beta})[55 - 66(\alpha^2 + \beta^2) + 90\alpha^2\beta^2 - 18(\boldsymbol{\alpha} \cdot \boldsymbol{\beta})^2]\}$$

References

[1] Vidal C R, Cooper J and Smith E W 1973 *Astrophys. J. Suppl.* **25** 37
[2] Griem H R 1974 *Spectral Line Broadening by Plasmas* (New York: Academic)
[3] Kelleher D E and Wiese W L 1973 *Phys. Rev. Lett.* **31** 1431
[4] Cooper J, Smith E W and Vidal C R 1974 *J. Phys. B: At. Mol. Phys.* **7** L101
[5] Wiese W L, Kelleher D E and Helbig V 1975 *Phys. Rev.* A **11** 1854
[6] Grützmacher K and Wende B 1977 *Phys. Rev.* A **16** 243
[7] Okasaka R, Nagashima M and Fukuda K 1977 *J. Phys. Soc. Japan* **42** 1339
[8] Grützmacher K and Wende B 1978 *Phys. Rev.* A **18** 2140
[9] Chotin J L, Lemaire J L, Marque J P and Rostas F 1978 *J. Phys. B: At. Mol. Phys.* **11** 371
[10] Frisch U and Brissaud A 1971 *J. Quant. Spectrosc. Radiat. Transfer* **11** 1753
    Brissaud A and Frisch U 1971 *J. Quant. Spectrosc. Radiat. Transfer* **11** 1767; 1974 *J. Math. Phys.* **15** 524
    Brissaud A, Goldbach C, Léorat J, Mazure A and Nollez G 1976 *J. Phys. B: At. Mol. Phys.* **9** 1129; 1147
[11] Seidel J 1977 *Z. Naturf.* **32a** 1195; 1207; 1979 *Z. Naturf.* **34a** 1385; 1980 *Z. Naturf.* **35a** 679
[12] Smith E W, Talin B and Cooper J 1981 *J. Quant. Spectrosc. Radiat. Transfer* **26** 229
[13] Stamm R and Voslamber D 1979 *J. Quant. Spectrosc. Radiat. Transfer* **22** 599
[14] Seidel J and Stamm R 1982 *J. Quant. Spectrosc. Radiat. Transfer* **27** 499

[15] Stamm R, Botzanowski Y, Kaftandjian V P, Talin B and Smith E W 1984 *Phys. Rev. Lett.* **25** 2217
[16] Stamm R and Smith E W 1984 *Phys. Rev.* **30** 450
      Stamm R, Smith E W and Talin B 1984 *Phys. Rev.* **30** 2039
[17] Gigosos M A and Cardeñoso V 1987 *J. Phys. B: At. Mol. Phys.* **20** 6006
[18] Hegerfeld G C and Kesting V 1988 *Phys. Rev.* A **37** 1488
[19] Gigosos M A and Cardeñoso V 1989 *J. Phys. B: At. Mol. Opt. Phys.* **22** 1743
[20] Cardeñoso V and Gigosos M A 1989 *Phys. Rev.* A **39** 5258
[21] Gigosos M A, Cardeñoso V and Torres F 1986 *J. Phys. B: At. Mol. Phys.* **19** 3027
[22] Greene R L 1982 *J. Quant. Spectrosc. Radiat. Transfer* **27** 639
[23] Oza D H, Greene R L and Kelleher D E 1986 *Phys. Rev.* A **34** 4519
[24] Oza D H, Greene R L and Kelleher D E 1988 *Phys. Rev.* A **37** 531
[25] Oza D H, Greene R L and Kelleher D E 1988 *Phys. Rev.* A **38** 2544
[26] Frerichs M R 1989 *Z. Phys.* D **11** 315
[27] Kelleher D E, Wiese W L, Helbig V, Greene R L and Oza D H 1993 *Phys. Scr.* T **47** 75
[28] Gigosos M A, Fraile J and Torres F 1985 *Phys. Rev.* A **31** 3509
[29] Hooper C F Jr 1968 *Phys. Rev.* **169** 193
[30] Demkov Y N, Monozon B S and Ostrovskii V N 1969 *Zh. Eksp. Teor. Fiz.* **57** 1431 (Engl. transl. 1970 *Sov. Phys.–JETP* **30** 775)
[31] Biedenharn L C, Louck J D and Carruthers P A 1981 Angular momentum in quantum physics: theory and application *Encyclopedia of Mathematics and its Applications* vol 8 (Reading, MA: Addison-Wesley)
[32] See [31], p 335
[33] Abramowitz M and Stegun A 1972 *Handbook of Mathematical Functions* (New York: Dover)
[34] Bethe H A and Salpeter E E 1957 *Quantum Mechanics of One- and Two-Electron Atoms* (Berlin: Springer)
[35] Lisitsa V S and Sholin G V 1972 *Sov. Phys.–JETP* **34** 484
[36] Greene R L, Cooper J and Smith E W 1975 *J. Quant. Spectrosc. Radiat. Transfer* **15** 1025
[37] Sahal-Brechot S 1969 *Astron. Astrophys.* **1** 91
[38] Grützmacher K and Wende B 1978 *IV Int. Conf. on Spectral Line Shapes (Windsor, Ontario)* Invited papers p 49, see also [6]
[39] Geisler M, Grützmacher K and Wende B 1980 *V Int. Conf. on Spectral Line Shapes (Berlin)* ed B Wende (Berlin: de Gruyter) p 103
[40] Stehlé C and Feautrier N 1984 *J. Phys. B: At. Mol. Phys.* **17** 1477
      Stehlé C 1990 *J. Quant. Spectrosc. Radiat. Transfer* **44** 135
[41] Wiese W L, Kelleher D E and Paquette D R 1972 *Phys. Rev.* A **6** 1132
[42] Ehrich H and Kusch H J 1973 *Z. Naturf.* **28a** 1794
[43] Ehrich H 1978 *Z. Naturf.* **34a** 188
[44] Weber E W, Frankenberger R and Schilling M 1983 *Appl. Phys.* B **32** 63
[45] Vitel Y 1987 *J. Phys. B: At. Mol. Phys.* **20** 2327
[46] Oza D H and Greene R L 1988 *J. Phys. B: At. Mol. Opt. Phys.* **21** L5
[47] Helbig V and Nick K P 1981 *J. Phys. B: At. Mol. Phys.* **14** 3573